Carbon Geochemistry of the Active Serpentinization Site at the Wadi Tayin Massif: Insights from the ICDP Oman Drilling Project – Phase II

Lotta Ternieten[1], Gretchen L Früh-Green[1] and Stefano M Bernasconi[1]

[1]Department of Earth Sciences, ETH Zurich, Clausiusstrasse 25, 8092, Zurich, Switzerland.

Corresponding author: Lotta Ternieten (lotta.ternieten@erdw.ethz.ch)

Key Points:

- Two carbonate occurrences are observed: localized dolomite, calcite, and aragonite veins and pervasive dispersed carbonates.
- Carbonate precipitation in the peridotite occurred in the last 50 kyr at moderate temperatures, post-dating ocean-floor serpentinization.
- The oxygen isotope composition of dispersed carbonates indicates precipitation from highly ^{18}O-depleted fossil groundwater.

Abstract

A large part of hydrated oceanic lithosphere consists of serpentinites exposed in ophiolites, which constitute reactive chemical and thermal systems and potentially represent an effective sink for CO_2. Understanding carbonation mechanisms is almost exclusively based on studies of outcrops, which can limit the interpretation of fossil hydrothermal systems. We present stable and radiogenic carbon data that provide insights into the isotopic trends and fluid evolution of peridotite carbonation in ICDP Oman Drilling Project drill holes BA1B (400 m deep) and BA3A (300 m deep). Geochemical investigations of the carbonates in serpentinites indicate formation in the last 50 kyr, implying a distinctly different phase of alteration than the initial oceanic hydration and serpentinization of the Samail Ophiolite. The oldest carbonates (~31 to > 50 kyr) are localized calcite, dolomite, and aragonite veins, which formed between 26 to 43 °C and are related to focused fluid flow. Subsequent pervasive small amounts of dispersed carbonate precipitated in the last 1000 yr. Macroscopic brecciation and veining of the peridotite indicate that carbonation is influenced by tectonic features allowing infiltration of fluids over extended periods of time and at different structural levels such as along fracture planes and micro-fractures and grain boundaries, causing large-scale hydration of the ophiolite. The formation of dispersed carbonate is related to percolating fluids with $\delta^{18}O$ lower than modern ground- and meteoric water. We also show that radiocarbon investigations are an essential tool to interpret the carbonation history and that stable oxygen and carbon isotopes alone can result in ambiguous interpretations.

Plain Language Summary

Water-rock interactions in biological and economically important settings has gained increasing interest of late. Carbon, stored in the atmosphere, terrestrial biosphere, oceans, and lithosphere, is profoundly affected by these exchange reactions. Carbon is an essential element for various abiotic and biotic reactions and, as CO_2 and CH_4, contributes to greenhouse gases. Unraveling water-rock reactions provide information for a solution to reduce global warming by transforming atmospheric CO_2 into carbonates and to better evaluate the potential for life within the lithosphere. This study uses samples recovered by drilling mantle sequences of the Wadi Tayin Massif and presents chemical data to evaluate carbon sources, speciation, and transformations. The Wadi Tayin Massif is located in the Samail Ophiolite and comprises mantle rocks. Mantle rocks react in contact with water to form serpentine and create an environment that promotes the transformation

of CO_2 into carbonates. Our results demonstrate large-scale carbonization of the Wadi Tayin Massif and a dominance of pervasive dispersed carbonate formation below the surface. The isotopic signal shows unique characteristics and organic carbon signatures similar to oceanic settings. Our study provides insights into the carbon cycle and will help to evaluate the potential of mantle rocks to store carbon and sustain life.

1 Introduction

Serpentinites make up a large part of the hydrated oceanic lithosphere and are exposed on the ocean floor and in ophiolites on continents, constituting highly reactive chemical and thermal systems. The alteration of oceanic lithosphere by hydrothermal fluids is the primary driver of hydrosphere – lithosphere volatile exchange and has significant consequences for rock physical properties and planetary-scale element fluxes (Beinlich, John, et al., 2020; Lister, 1972; Wheat & Mottl, 2004). Carbon – as one of the most important elements on Earth – is stored in ultramafic rocks in the form of gaseous CO_2, and CH_4 in fluid inclusions, as solid inorganic carbonate and graphite, and as organic compounds that can be abiotically or biotically produced (Delacour, Früh-Green, Bernasconi, Schaeffer, et al., 2008; Kelley & Früh-Green, 2001; McCollom & Seewald, 2006). C-bearing species have multiple origins and can persist in ancient mantle domains over extended periods. Previous studies have shown that the speciation, concentration, and isotopic composition of carbon provide information about the chemical and physical conditions of the reservoir and the dominant physical, chemical, and/or biological processes in the system (Arai et al., 2012; Charlou et al., 2002; Delacour, Früh-Green, Bernasconi, & Kelley, 2008; Kelley et al., 2005; Schwarzenbach, Früh-Green, et al., 2013; Shanks et al., 1995).

Recent studies have shown that microbial life can be sustained within the lithosphere by fluid-mediated chemical reactions that provide utilizable energy resources, which implies that the deep subsurface biosphere may be the largest microbial habitat on Earth (Barry et al., 2019; Colman et al., 2017; Fullerton et al., 2019). For example, hydrothermal circulation of fluids have been postulated to liberate CH_4-rich fluids from intrusive rocks in the oceanic lithosphere (e.g., Labidi et al., 2020; Wang et al., 2018) and redox reactions during the formation of serpentine from mantle olivine and pyroxene generate substantial amounts of H_2 (McCollom & Bach, 2009). Production of H_2 by serpentinization has been identified at mid-ocean ridges (Cannat et al., 2010; Früh-Green et al., 2004; Kelley et al., 2005; Konn et al., 2015), as well as on-land (Etiope & Sherwood Lollar, 2013) and in the shallow forearc of subduction zones (Mottl et al., 2003; Ohara et al., 2012). Metagenomic studies of serpentinization-fueled hydrothermal deep-sea vents and continental fluid seeps provide evidence for microbial H_2 and CH_4 utilization in these harsh environments where nutrient and electron acceptor availability may be limited by high pH, which in turn depends on the temperature of the system (Brazelton et al., 2012; Curtis et al., 2013; Ohara et al., 2012; Schrenk et al., 2013).

Hydration of mantle peridotites can also be associated with the storage of carbon in large carbonate deposits. Serpentinization at temperatures below approximately 200 °C produces fluids with high Ca^{2+} concentration and high pH, which can lead to carbonate precipitation (Frost & Beard, 2007; Palandri & Reed, 2004). Natural carbon uptake in thermodynamically stable carbonate may represent a means for permanently removing CO_2 from the atmosphere (Kelemen & Matter, 2008) and may help stabilize atmospheric greenhouse gas concentrations over long timescales. The carbon uptake potential is particularly strong in the ultramafic part of the oceanic lithosphere that has previously equilibrated under dry high-temperature conditions and has high concentrations of divalent metal ions required for carbonate mineral formation (Kelemen et al., 2011). The resulting carbonate minerals are typically accompanied by secondary silicates and Fe-oxide, hydroxide, and/or sulfide phases. An extreme endmember of carbonation is listvenite, which forms where extensive infiltration of CO_2- rich fluids alter ultramafic rocks and where almost the entire inventory of Mg and Ca cations are incorporated into carbonate minerals (Halls & Zhao, 1995).

To better evaluate the potential of ultramafic rocks as long-term storage for CO_2, quantitative information on the sources and sinks of carbon is necessary. One critical factor contributing to continuing uncertainty is the difficulty in obtaining samples directly from subsurface environments near mid-ocean ridges. Consequently, most estimates are based on information inferred from analysis of hydrothermal fluids discharged at the seafloor. One possibility to bypass this problem is to study ophiolites. One of the largest and best explored carbonated ophiolite complexes is the Samail Ophiolite in the Sultanate of Oman and the United Arab Emirates, which includes massifs in the south that represent relics of a mid-ocean ridge (Chavagnac et al., 2013; Clark & Fontes, 1990; Falk et al., 2016; Falk & Kelemen, 2015; Hanghoj et al., 2010; Kelemen & Matter, 2008; Mervine et al., 2014; Nasir et al., 2007; Neal & Stanger, 1983, 1985; Paukert et al., 2012; Stanger, 1985; Streit et al., 2012).

The Samail Ophiolite comprises a complete sequence of the oceanic lithosphere from the upper mantle through to the oceanic crust, all of which have recently been the target of comprehensive drilling and subsequent analysis of rock core, logging, hydrological and microbial sampling in the course of the Oman Drilling Project (OmanDP) (Kelemen, Matter, Teagle, et al., 2020). We present petrographic and carbon and oxygen isotope analyses from two holes, Holes BA1B and BA3A of the OmanDP, which recovered serpentinized dunites and harzburgites that

are variable carbonated, to better constrain the conditions and reaction pathways driving alteration and carbonation at a large scale. Mineralogy, isotopic trends, carbon sources, and speciation are discussed to constrain critical reaction parameters and chemical equilibration during natural large-scale hydration and carbonization. In addition, our study aims to characterize biogenic and abiogenic processes controlling carbon cycling within the Samail Ophiolite and evaluate the potential for long-term storage for CO_2.

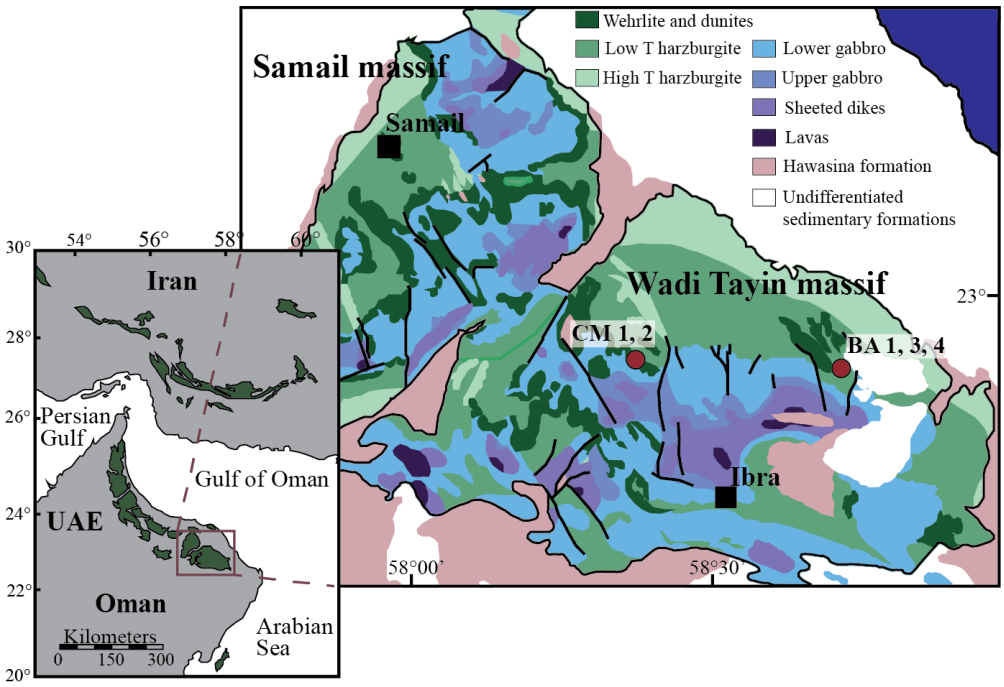

Figure 1. Geological map of the Samail and Wadi Tayin Massifs, Samail ophiolite, modified after Nicolas et al. (2000) and Hanghoj et al. (2010) showing the locations of the study sites BA (active serpentinization) and CM (crust-mantle boundary) of the Oman Drilling Project - Phase II (red circles) (Kelemen, Matter, Teagle, et al., 2020).

2 Geological Setting and Sampling

The Samail Ophiolite consists of approximately 15 massifs and is the most extensive and best-exposed cross-section through the oceanic lithosphere (Figure 1). The ophiolite comprises an intact stratigraphy of Penrose-type layered oceanic crust and mantle composed of pelagic

allochthonous sediments, overlying pillow basalts, a sheeted dike complex, gabbros, and upper mantle peridotite (Coleman, 1981; Searle & Malpas, 1980). The metamorphic sole underneath the ophiolite sequence consists of metaphyllites, greenschist facies metabasalts, and minor amphibolites of the Haybi Complex (Searle & Malpas, 1980). The metamorphic sole is underlain by Permian to Late Cretaceous pelagic sediments, meta-volcanic rocks, and shelf-facies limestone of the Hawasina Group, which appear as tectonic windows between the ophiolitic massifs (Figure 1) (Coleman, 1981; Nasir et al., 2007; Searle et al., 2015; Stanger, 1985).

The oceanic lithosphere formed most likely at a medium- to fast-spreading ridge like the East Pacific Rise (EPR) or the Juan de Fuca Ridge (Nicolas, 1989; Tilton et al., 1981). U–Pb dating of magmatic zircon and $^{40}Ar/^{39}Ar$ ages of mica and hornblende from the metamorphic sole indicate that thrusting of the Samail Ophiolite onto the autochtonous Proterozoic to Mesozoic sedimentary Arabian continental margin occurred between 95 Myr and 71 Myr (Cowan et al., 2014; Gnos, 1998; Hacker, 1994; Hacker et al., 1996; Hacker & Gnos, 1997; Hacker & Mosenfelder, 1996; Lanphere, 1981; Rabu et al., 1993; Rioux et al., 2016, 2012, 2013; Tilton et al., 1981; Warren et al., 2005). During this time, the ophiolite was repeatedly under shallow seawater or emerged above sea level caused by oscillating transgression-regression cycles (e.g., Coleman, 1981).

2.1 Samail and Wadi Tayin Massif

The southern massifs of the Oman ophiolite complex, known as the Samail and Wadi Tayin Massifs, were formed primarily via a MORB-like, single-stage process at a submarine spreading ridge (Godard et al., 2003). Outcrops of the crustal and mantle sequence can be found at both massif; however, the structural thickness of the mantle section differs between the Samail and the Wadi Tayin Massif with 4 km and over 10 km, respectively (Hanghoj et al., 2010; Nicolas et al., 2000). The extensive mantle sequence at the Wadi Tayin Massif is overlain by a 5 to 7 km thick crustal gabbro section, sheeted dikes, and pillow lavas (Figure 1). The mantle section of the southern massifs comprises mainly harzburgite and minor lherzolite that host 5 to 15 % dunites and contains multiple mafic intrusions (Boudier & Coleman, 1981; Pallister & Knight, 1981).

The harzburgites record ‘near fractional’ partial melt extraction and are geochemically similar to abyssal peridotites (Godard et al., 2000; Kelemen et al., 1995; Le Mée et al., 2004; Monnier et al., 2006). Dunites represent channels of focused melt transport through the harzburgites, with a thickness of < 1cm to 100 m or more, and were formed by melt-rock

interaction between MORB-like melts and harzburgite (Braun, 2004; Braun & Kelemen, 2002; Kelemen et al., 1995). Gravity anomalies (Ravaut et al., 1997) suggest that the Samail and Wadi Tayin Massifs are composed of 30 – 60 % (locally reaching 100 %, Falk & Kelemen, 2015) serpentinized mantle peridotite, extending up to 5 km below the present-day surface. In addition, listvenites are observed at the base of the ophiolitic mantle section, which are formed at high temperatures during subduction by the reaction with CO_2-rich, sediment-derived fluids (Falk & Kelemen, 2015). However, there is still debate whether the southern massifs were formed at a 'normal' mid-ocean ridge (Braun, 2004), in a supra-subduction zone setting, or via unique processes during ophiolite obduction (Hanghoj et al., 2010; Kelemen, Matter, Teagle, et al., 2020). For instance, there are some differences compared to typical spreading ridges, such as slightly high Th/Nb and SiO_2 in some lavas (Hanghoj et al., 2010) and higher spinel Cr-number in some peridotites (Dick & Bullen, 1984) of the Wadi Tayin Massif.

Tectonic uplift and erosion of the southern massif mantle rocks lead to extensive ongoing serpentinization of the peridotite by groundwaters (Kelemen et al., 2011; Kelemen & Matter, 2008; Paukert et al., 2012). The reaction of groundwaters with peridotite at low temperatures forms (i) medium pH ~8, Mg-HCO_3^- -rich, oxidized fluids in the near-surface (defined as Type I fluids by Barnes & O'Neil, 1969; Bruni et al., 2002; and Dewandel et al., 2005) and when isolated from the atmosphere at greater depth, (ii) high pH ~12, Ca-OH -rich, highly reduced fluids with no dissolved carbon or Mg^{2+} (Type II fluids) are formed (Neal & Stanger, 1985). These fluids mixed with dissolved inorganic carbon (DIC: $CO_{2(aq)} + HCO_3^- + CO_3^{2-}$) or in contact with atmospheric $CO_{2(g)}$ can lead to a large volume of carbonates. Previous studies showed that travertine and vein formation occurred at 20 to 60 °C and that their ^{14}C ages ranged from modern to > 50 kyr with an average of about 26 kyr (Clark & Fontes, 1990; Kelemen et al., 2011; Kelemen & Matter, 2008; Streit et al., 2012).

2.2 The Oman Drilling Project – Phase II

Phase II of the OmanDP drilled nine boreholes (from 300 to maximum 400 m deep) at two sites in the Wadi Tayin Massif and targeted the crust-mantle transition zone (CM) and an active alteration zone (BA) in mantle peridotites (Figure 1). The OmanDP aims to establish a multi-borehole observatory to address a spectrum of questions that connect the deep mantle and the ancient ocean floor with modern hydrology and ongoing biogeochemical reactions in the

mountains and wadis of the Samail Ophiolite. Our study focuses on the active alteration Site BA, which targets hydration and carbonization at temperatures < 50 °C and provides an excellent opportunity to better understand how alteration and serpentinization are coupled to the carbon cycle.

Drilling at Site BA included three diamond cored (BA3A, BA1B, and BA4A) and two rotary drill holes (BA1C and BA1D). Drill cores of the OmanDP – Phase II are described in detail in Kelemen, Matter, Teagle, et al. (2020). We focus on the two Holes BA1B and BA3A from the mantle section of the ophiolite (Figure 2). The ultramafic rocks from Site BA reveal a high and heterogeneous degree of serpentinization, several pyroxenite and gabbroic dykes, in parts extended oxidation zones, and local rodingitization (Kelemen, Matter, Teagle, et al., 2020). Contacts between ultramafic and mafic domains are marked by chlorite, prehnite, talc, and hydrogrossular, indicating metasomatism on a millimeter scale. A recent *in-situ* oxygen isotope study of the serpentinites from Hole BA1B defined three distinct stages of hydration (Scicchitano et al., 2020): (i) seafloor serpentinization at temperatures of up to approximately 190 °C, followed by (ii) serpentinization caused by infiltration of meteoric water with δ^{18}O value of ~ -7 ‰ at 32 °C, and (iii) ongoing serpentinization also at 30 to 33 °C by ground- and/or meteoric water with δ^{18}O value of ~ -0.7 ‰. Carbonate-rich zones occur in the upper 150 m and are characterized by a distinct decrease in vein abundance with depth. Cores had 100 % recovery; in BA1B, they consist of ~55 % harzburgite, ~35 % dunite and ~10 % mafic dykes and alluvium, and in BA3A, ~97 % harzburgite and less than 3 % mafic dykes and alluvium were recoverd (Figure 2).

3 Materials and Methods

Isotopic investigations were made on 26 harzburgites and nine dunites from Holes BA1B and BA3A, covering the diversity of rock types and alteration. In addition, we measured clumped isotopes on 21 carbonate veins from 19 serpentinized peridotites. Petrographic investigations were made on 20 doubly polished thin sections of representative samples from Hole BA1B. Detailed information on the samples is given in Tables 1 and 2. A simplified lithostratigraphy is shown in Figure 2. Samples are named after ICDP guidelines: Expedition_Site, Hole (Chikyu Hole)_Core, Coretype_Section_Interval in cm; (e.g., 5057_BA1B (5B)_75Z_1_39-90). For simplicity, we have removed the expedition number "5057," which is the same for all samples, and the Chikyu Hole information (the example above is thus reported as BA1B_75Z_1_39-90). The depth below the

present-day surface is given in meters and defined as the Chikyu Adjusted Depth (CAD). Details of the depth computations are given in Kelemen, Matter, Teagle., et al. (2020), Methods, and explanatory notes.

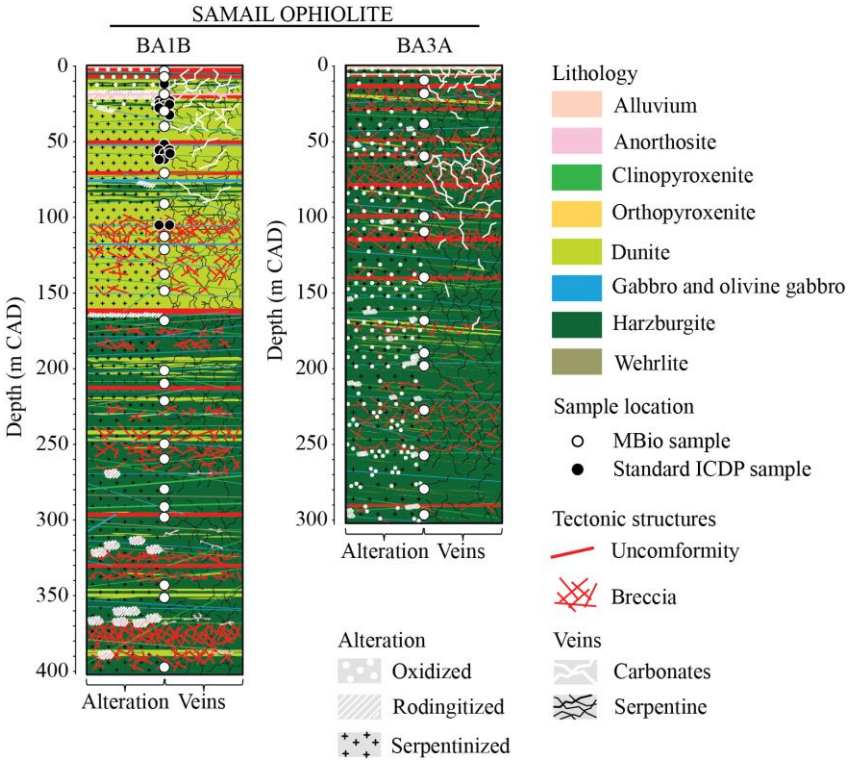

Figure 2. Simplified downhole logs (meters Chikyu Adjusted Depth = m CAD) of the dominant lithologies and tectonic features recovered in Holes BA1B and BA3A of the OmanDP containing serpentinized peridotites. BA1B consist of 160 m of dunite on top, followed by 240 m of harzburgite. BA3A contains 300 m of harzburgite. Both holes are cut by multiple gabbroic intrusions (modified after Kelemen, Matter, Teagle, et al., 2020). The white dots indicate locations of MBio samples, and the black dots indicate locations of standard ICDP samples (sampled under non-sterile conditions).

3.1 Sample Preparation

Sample preparation depended on whether the samples were aliquots of samples used for microbiological studies and were collected under sterile conditions (denoted as MBio samples) used for whole-rock analyses or whether the samples were obtained using standard ICDP protocols (denoted as standard ICDP samples) for analyses of carbonate veins and petrographic studies. In the field, the MBio dedicated cores were washed on the outside with ultraclean deionized water and cut using a diamond blade saw lubricated with deionized water. For subsampling, the subcore was transferred onto combusted foil and crushed using an ethanol-washed hammer, chisel, and tweezers. Finally, the MBio subsamples were transferred into a N_2 glovebox, washed twice with N_2-purged deionized water, wrapped in foil, sealed into mylar bags flushed with N_2 together with an O_2-scrubbing sachet (BD GasPak 260001), and stored at 4 °C. A description of sample handling procedures during the OmanDP can be found in the OmanDP methods in Kelemen, Matter, Teagle., et al. (2020). In our laboratory, the MBio samples (rock chips or core pieces) were cleaned in the first step by ultrasonication in 100 ml dichloromethane (DCM) for 5 min at room temperature and subsequently dried for 24 h at room temperature in a pre-combusted glass container covered with combusted aluminum foil. The rock chips were then crushed, centerpieces collected and ground by hand using an agate mortar cleaned with DCM to obtain a homogenous powder.

We conducted whole-rock analyses to determine concentrations of total carbon (TC), total inorganic carbon (TIC), and total non-carbonate carbon (NCC), and the isotopic compositions ($\delta^{13}C$ and $\delta^{18}O$) of TIC, total carbon ($\delta^{13}C_{TC}$), and total non-carbonate (acid-insoluble) carbon ($\delta^{13}C_{NCC}$). TIC represents all inorganic carbon from a whole-rock powder (including potential carbonate veins) that reacts at room temperature within 24 h with 6M hydrochloric acid (HCl). Total NCC represents all remaining acid-insoluble carbon phases, including organic compounds, amorphous carbon, graphite, etc.; this carbon fraction is commonly reported collectively as total organic carbon (TOC) (e.g., Delacour, Früh-Green, Bernasconi, Schaeffer, et al., 2008).

The NCC and $\delta^{13}C_{NCC}$ were determined on 200 mg aliquots decarbonated with 3 ml of 6M hydrochloric acid (HCl). The remaining material was rinsed several times with Milli-Q water, dried at 70 °C overnight, and re-homogenized by hand using an agate mortar. 9 carbonate veins in samples obtained using standard ICDP protocols (denoted as samples) were used for clumped isotopes and radiocarbon dating. In a first step, the standard ICDP samples were cleaned with 2-

propanol and compressed air. Later, the surfaces of the veins were removed and discarded, followed by sampling of the veins with a hand-held drill. Additionally, 12 samples of loose carbonate crystals were hand-picked from larger carbonate veins, cleaned by ultrasonication in 100 ml dichloromethane (DCM) for 5 min at room temperature, and subsequently dried for 24 h at room temperature in a pre-combusted glass container covered with combusted aluminum foil. The carbonate samples were homogenized by hand using an agate mortar cleaned with DCM.

3.2 Powder X-ray Diffraction

Crystallographic analyses were made using a Bruker AXS D8 Advance Powder X-ray Diffractometer (XRD) equipped with a Lynxeye superspeed detector (Bruker Corporation, Billerica, United States) with Cu Kα radiation, a voltage of 45 kV, and a current of 40 mA, with 2θ ranging between 10° to 60° with a step size of 0.01°, and measurement time of 1 s per step. Quantification of the mineralogy was carried out using the program PowDll (Kourkoumelis, 2013) and the RRUFF database (Lafuente et al., 2015).

3.3 Optical Microscopy

Petrographic analyses were conducted using a polarizing microscope (Carl Zeiss Microscopy GmbH, Göttingen, Germany) and with a cold cathode cathodoluminescence (CL) CL8200 Mk5-2 (Cambridge Image Technology Ltd, Hertfordshire, UK). CL operating conditions were an accelerating voltage of 15 kV with a beam current of 250 to 300 µA.

3.4. Carbon Content and Isotopic Composition

TC and NCC contents and isotopic compositions were determined by combustion of 40 to 60 mg of a sample using a FlashEA 1112 Elemental Analyzer (EA) interfaced via a Conflo IV to a Delta V Plus Isotope Ratio Mass Spectrometer (MS) (all ThermoFisher Scientific, Bremen, Germany). The carbon content was calculated using two standards (Bodenstandards No.5; 0.141 %C, HEKAtech, Wegberg, Germany, and nicotinamide; 59.01 %C, ThermoFisher Scientific, Milan, Italy). Empty tin capsules were measured for blank correction. Analytical reproducibility of $\delta^{13}C_{TC}$ and $\delta^{13}C_{NCC}$ is ± 0.11 ‰ (1σ). The detection limit for a reproducible carbon isotope measurement is about 1 µg C. Carbonate contents determined as total inorganic carbon, TIC, were calculated by mass balance using Equation 1.

$$(f_{TC} * c_{TC}) = (f_{TIC} * c_{TIC}) + (f_{NCC} * c_{NCC}) \quad \text{(Eq.1)}$$

$\delta^{13}C$ and $\delta^{18}O$ of TIC were measured on a GasBench II connected to a Delta V mass spectrometer (both ThermoFisher Scientific, Bremen, Germany), as described in detail in Breitenbach & Bernasconi (2011). The average long-term reproducibility based on replicated standards is ± 0.10 ‰ for $\delta^{13}C$ and 0.11 ‰ for $\delta^{18}O$ (1σ). The instrument is calibrated with the international standards NBS19 ($\delta^{13}C$ = 1.95 ‰ and $\delta^{18}O$ = -2.2 ‰) and NBS18 ($\delta^{13}C$ = -5.01 ‰ and $\delta^{13}O$ = -23.01 ‰). Samples as small as ~20 µg TIC can be analyzed with confidence and the precision mentioned above and are reported as replicates. We performed several test runs on cryptocrystalline magnesite collected at the Wadi Tayin Massif to guarantee a complete reaction of the carbonates in the bulk rock samples.

A subset of carbonate veins was analyzed for clumped isotopes (Δ47) on a Kiel IV carbonate device interfaced with a ThermoFisher Scientific MAT253 isotope ratio mass spectrometer following the methodology described in detail in Meckler et al. (2014), and Müller et al. (2017). Briefly, 100 to 110 µg of carbonate were reacted with three drops of 104 % phosphoric acid (H_3PO_4) at 70 °C. The evolved CO_2 was purified on a custom-built Porapak Q trap held at -40 °C and measured on a MAT253 in micro-volume mode using the LIDI Protocol (Hu et al., 2014; Müller et al., 2017). The results are converted to the Carbon Dioxide Equilibrium Scale (CDES) using the carbonate standards ETH-1, ETH-2, and ETH-3 as described in Bernasconi et al. (2018). Dolomite values are reported for a reaction temperature of 70 °C, the same temperature used to establish the calibration of Müller et al. (2019), and calcites are projected to 25 °C. With 8 to 10 replicate analyses, the margins of error are ± 3 to 5 °C at the 95 % confidence level (CL) (Fernández et al., 2017). $\delta^{13}C$ and $\delta^{18}O$ of TIC and $\delta^{13}C$ of TC and NCC are reported in conventional delta notation with respect to the Vienna Pee Dee Belemnite (VPDB) standard.

Clumped isotopes allow the calculation of the $\delta^{18}O$ of the fluid equilibrated with the carbonate vein. We used the calibration of Grossman & Ku (1986) for aragonite, O'Neil et al. (1969) corrected by Friedman & O'Neil (1977) for calcites, and Müller et al.,(2019) for dolomites. The uncertainty for the calculated water $\delta^{18}O$ depends strongly on the number of possible replicate measurements, which control the uncertainty of the clumped isotope temperatures.

Table 1. Content and carbon (VPDB) and oxygen (VPDB) isotope compositions in total carbon (TC), total non-carbonate carbon (NCC), and total inorganic carbon (TIC) and estimated formation temperature of ultramafic rocks from the Wadi Tayin Massif at the Samail Ophiolite.

Site	Hole	Core	Section	Interval (cm)		Depth (m CAD)		Lithology	TC	NCC	TIC*	$\delta^{13}C_{TC}$	$\delta^{13}C_{NCC}$	$\delta^{13}C_{TIC}$	$\delta^{18}O_{TIC}$	T^a
				top	bot.	top	bot.		(ppm)	(ppm)	(ppm)	(‰)	(‰)	(‰)	(‰)	(°C)
BA	1B	2	2	27	35	4	4	Serpentinized harzburgite	1300	165	1325	-9.47	-25.87	-9.74	-1.99	9 to 59
BA	1B	3	2	73	85	7	7	Serpentinized dunite	13608	139	13782	-12.02	-26.14	-12.07	-2.82	13 to 65
BA	1B	7	2	21	63	19	19	Serpentinized dunite	296	182	268	-10.43	-26.59	-7.57	-13.51	72 to 167
BA	1B	11	1	6	33	30	30	Serpentinized dunite	1619	136	1722	-10.59	-24.10	-10.90	-11.25	57 to 137
BA	1B	20	3	0	50	40	41	Serpentinized dunite	1489	222	1796	-8.85	-25.64	-11.55	-15.80	88 to 204
BA	1B	31	4	0	53	71	71	Serpentinized harzburgite	736	207	773	-9.18	-26.12	-9.75	-11.50	59 to 140
BA	1B	38	2	0	50	91	91	Serpentinized dunite	399	196	415	-11.52	-27.04	-13.07	-11.94	62 to 146
BA	1B	45	4	0	49	113	114	Serpentinized dunite	786	175	733	-8.57	-26.60	-8.02	-14.29	77 to 178
BA	1B	48	2	11	60	121	121	Serpentinized dunite	1011	263	1167	-9.00	-26.17	-11.72	-14.51	79 to 182
BA	1B	54	2	0	49	138	139	Serpentinized dunite	569	191	636	-10.65	-26.48	-12.51	-11.92	62 to 146
BA	1B	57	3	0	50	149	149	Serpentinized dunite	844	221	1041	-9.77	-21.61	-13.36	-14.05	76 to 175
BA	1B	64	3	0	50	169	170	Serpentinized harzburgite	651	191	681	-12.55	-27.81	-15.02	-14.58	79 to 183
BA	1B	75	1	39	90	201	202	Serpentinized harzburgite	1032	297	967	-11.37	-29.64	-11.17	-13.96	75 to 173
BA	1B	78	1	48	96	210	211	Serpentinized harzburgite	918	206	1047	-7.24	-26.27	-9.95	-14.48	79 to 181
BA	1B	81	4	0	51	221	222	Serpentinized harzburgite	590	238	508	-11.05	-27.37	-11.07	-14.68	80 to 185
BA	1B	91	3	0	52	250	251	Serpentinized harzburgite	511	299	379	-14.23	-27.91	-11.69	-14.45	78 to 181
BA	1B	94	4	0	53	260	261	Serpentinized harzburgite	750	358	520	-15.90	-28.94	-14.37	-14.71	80 to 185
BA	1B	101	2	21	76	280	281	Serpentinized harzburgite	467	200	388	-10.97	-25.73	-10.56	-14.37	78 to 180
BA	1B	105	1	10	57	291	291	Serpentinized harzburgite	542	286	456	-9.23	-25.74	-8.26	-14.80	81 to 187
BA	1B	107	4	0	55	299	300	Serpentinized harzburgite	721	245	747	-9.57	-24.90	-11.24	-13.68	73 to 169
BA	1B	122	2	0	50	343	343	Serpentinized harzburgite	750	265	750	-8.78	-27.98	-9.80	-13.94	75 to 173
BA	1B	125	1	47	97	351	352	Serpentinized harzburgite	593	126	601	-9.15	-27.06	-10.66	-13.58	72 to 168
BA	1B	141	4	0	53	398	399	Serpentinized harzburgite	723	337	641	-11.18	-26.88	-9.77	-14.55	79 to 183
BA	3A	7	2	0	35	10	10	Serpentinized harzburgite	1241	218	1424	-7.17	-22.07	-9.09	-11.53	59 to 141
BA	3A	12	2	32	85	19	19	Serpentinized harzburgite	1220	239	1019	-8.89	-24.04	-5.90	-14.85	81 to 188
BA	3A	19	2	0	55	39	40	Serpentinized harzburgite	752	300	1185	-6.30	-24.06	-12.79	-12.91	68 to 158
BA	3A	27	1	28	88	60	61	Serpentinized harzburgite	1242	349	1100	-7.98	-23.79	-5.94	-12.34	64 to 151
BA	3A	43	2	32	83	100	100	Serpentinized harzburgite	738	170	703	-5.78	-27.99	-4.67	-11.61	60 to 142
BA	3A	46	3	39	86	110	110	Serpentinized harzburgite	1232	473	1226	-6.15	-25.94	-6.05	-12.12	63 to 148
BA	3A	58	3	38	95	140	140	Serpentinized harzburgite	1052	206	1038	-7.26	-26.14	-7.01	-12.88	68 to 158
BA	3A	69	3	25	77	169	170	Serpentinized harzburgite	906	137	874	-9.10	-25.88	-8.47	-11.97	62 to 146
BA	3A	76	3	0	50	190	191	Serpentinized harzburgite	1175	479	1194	-8.15	-27.24	-8.45	-13.29	71 to 164
BA	3A	79	2	41	93	199	200	Serpentinized harzburgite	215	158	191	-8.77	-25.55	-6.60	-15.12	83 to 192
BA	3A	89	1	36	85	228	229	Serpentinized harzburgite	1131	429	1231	-9.33	-27.28	-10.79	-13.80	74 to 171
BA	3A	99	1	24	76	258	258	Serpentinized harzburgite	1100	214	1141	-9.00	-24.14	-9.55	-12.62	66 to 155
BA	3A	106	2	0	50	280	280	Serpentinized harzburgite	1084	235	1193	-9.54	-25.36	-10.99	-14.21	77 to 177
BA	3A	113	2	0	49	297	298	Serpentinized harzburgite	971	332	920	-7.89	-27.32	-6.81	-14.13	76 to 176

* Calculated inorganic carbon content using equation 1; [a] Range of calculated oxygen isotope temperatures

3.5 Radiocarbon Ages

Radiocarbon ages of decarbonated samples were measured by combustion with an Elemental Analyzer interfaced to a MICADAS Accelerator Mass Spectrometer (AMS) (Synal et al., 2007) equipped with gas-ion source at the Laboratory of Ion Bean Physics, ETH Zurich (Ruff et al., 2010; Wacker et al., 2010). Whole-rock TIC and carbonate veins were measured by reaction with phosphoric acid reaction in vacutainers that were previously purged for 10 minutes with He, followed by direct injection of the produced CO_2 into the ion source of the AMS. The results are normalized against standard Oxalic Acid II (NIST SRM 4990C) and corrected with a radiocarbon blank CO_2 (IAEA C-1). In addition, IAEA-C2 and coral CSTD were measured in each run to test the accuracy of the measurement. The precision was better than ± 5 ‰ on a modern standard. Radiocarbon data are expressed as $F^{14}C$ (fraction of modern carbon) and conventional ^{14}C ages, according to Reimer et al. (2004). $F^{14}C$ of the TIC was calculated by mass balance using $F^{14}C$ and content of total carbon and total non-carbonate carbon.

4 Results

One of the main differences between the two studied boreholes is the distinct amounts of dunite and carbonate veins (Figure 2). Hole BA1B drilled through 160 m of dunites at the top, followed by a 240 m thick harzburgite sequence. Hole BA3A drilled through 300 m of harzburgites without a major dunite sequence. The serpentinized dunites from Hole BA1B contain complex networks of distinct generations of aragonite, calcite, and dolomite veins. In Hole BA3A, carbonate veins were found only in the uppermost ~5 m.

4.1 Carbonate Occurrences

Carbonates in the mantle rocks from the Wadi Tayin Massif occur as (i) veins, (ii) as replacement of serpentine after pyroxene and olivine (Figure 3), (iii) and as finely dispersed grains in the serpentinites. Carbonate veins were observed in both mafic and ultramafic rocks within the dunitic sequence of Hole BA1B, where they can make up to ~ 30 vol% of a rock sample in some shallow and oxidized rocks (Figure 3a). An example of the size of a sample from the rock cores is given in Figure 3b.

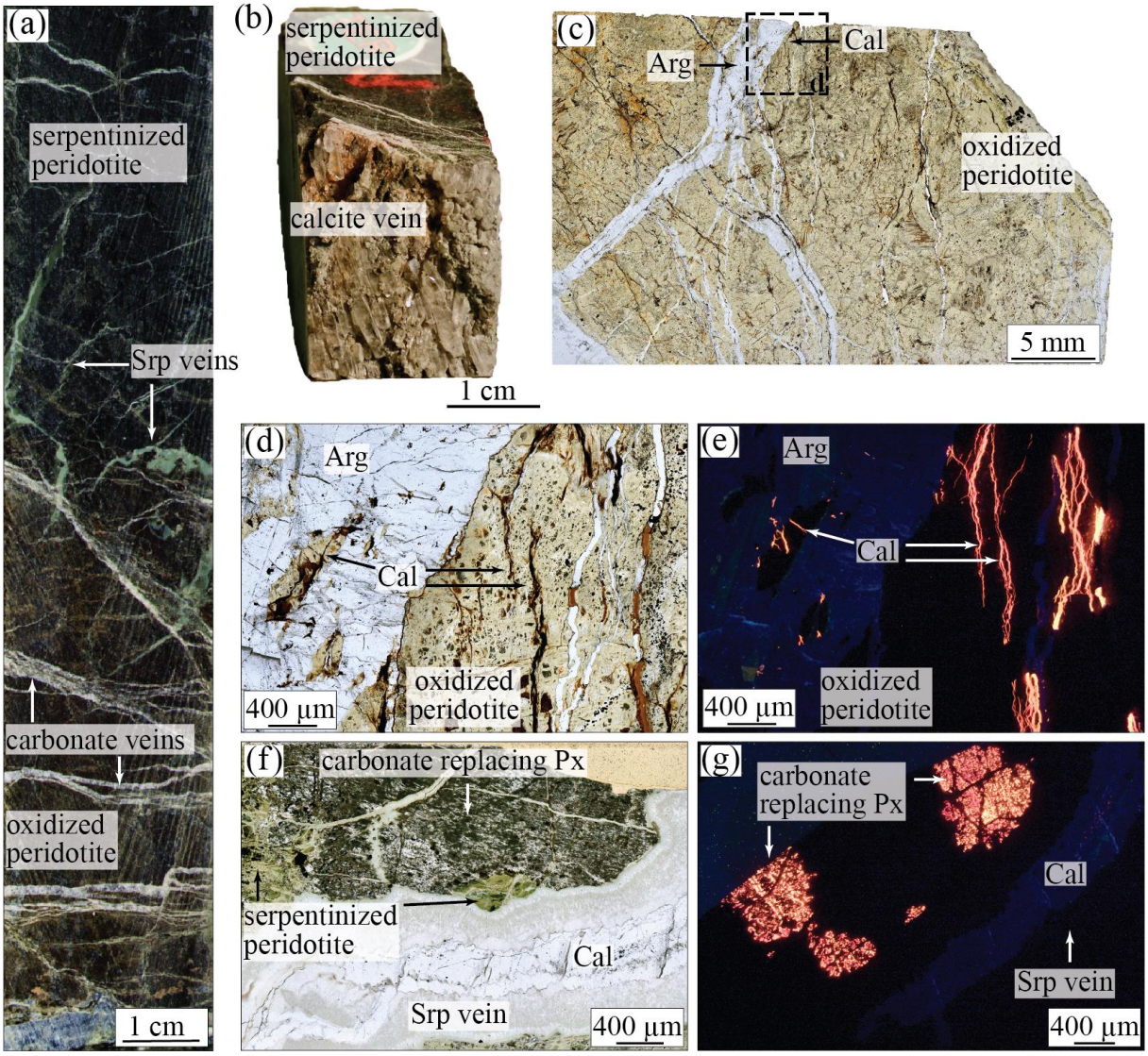

Figure 3. Core scan and photomicrographs showing typical host lithologies and carbonates in the BA1B drillcore. (a) The core of fully serpentinized dunite with multiple carbonate veins in a highly oxidized domain. The top of the core is less oxidized and contains fewer carbonate veins (sample BA1B_14M_3_68-82). (b) Large euhedral calcite crystals in a fracture of fully serpentinized dunite (BA1B_10Z_3_4-6). (c) Aragonite and Mg-rich calcite veins in serpentinized dunite. (d) Close-up of Fig. 2c showing serpentinized dunite crosscut by aragonite veins, which contain an earlier Mg-rich calcite vein generation (sample BA1B_4Z_4_12-17). (e) CL-image of the serpentinized dunite from Fig. 2d showing non-luminescent aragonite and

360 calcite with a strong orange CL. (f) Carbonates replace serpentine after pyroxene within a
361 serpentinized peridotite and calcite reactivating serpentine vein (BA1B_17Z_1_17-22, PPL). (g)
362 CL-image of carbonates replacing highly altered pyroxene within serpentinized peridotite and
363 calcite reactivating serpentine vein. Abbreviations: Arg, aragonite; Cal, calcite; Px, pyroxene;
364 Srp, serpentine.

365

366 Carbonate veins are typically less than 1 cm wide, dissect grain boundaries, have kinked
367 to irregular shapes, and show crosscutting or, more rarely, branching geometries. They crosscut
368 all other textures, indicating a late stage of formation (Figures 3b - e), and are composed of
369 aragonite, calcite, and dolomite in variable proportions. In some samples, at least two generations
370 of carbonates coexist in the same rock (Figures 2c - e). Dolomite veins are < 2 mm wide and are
371 found only in the top 25 m and 5 m of the Holes BA1B and BA3A, respectively. Calcite veins are
372 more common, are a few mm wide (Figures 3b - g), and occur in the top 110 m at Hole BA1B.
373 The most abundant and volumetrically dominant carbonate type are up to 1 cm wide aragonite
374 veins in the top 33 m of Hole BA1B. The aragonite occurs in veins that crosscut the primary rock
375 fabric (Figures 2c - d), postdate all secondary fabrics, and are the last carbonate vein to form.

376 Carbonates replacing serpentine mesh cores after pyroxene and olivine occur in the top 33
377 m of Hole BA1B; these are dominantly calcite and have an average grain size < 20 µm (Figures
378 2f - g). Dispersed carbonates could not be identified microscopically but are indicated by whole-
379 rock concentration and isotopic measurements and occur throughout the cores of both drill holes.

380 4.2 Carbon Isotopes

381 4.2.1 Bulk Rock Carbon in the Basement Rocks

382 The studied rocks show a wide range of total carbon contents, mainly reflecting varying
383 carbonate abundance. Total carbon ranges from 215 ppm to 1.4 wt% with $\delta^{13}C_{TC}$ values from -
384 15.9 to -5.8 ‰ (Table 1, Figures 4 and 5).

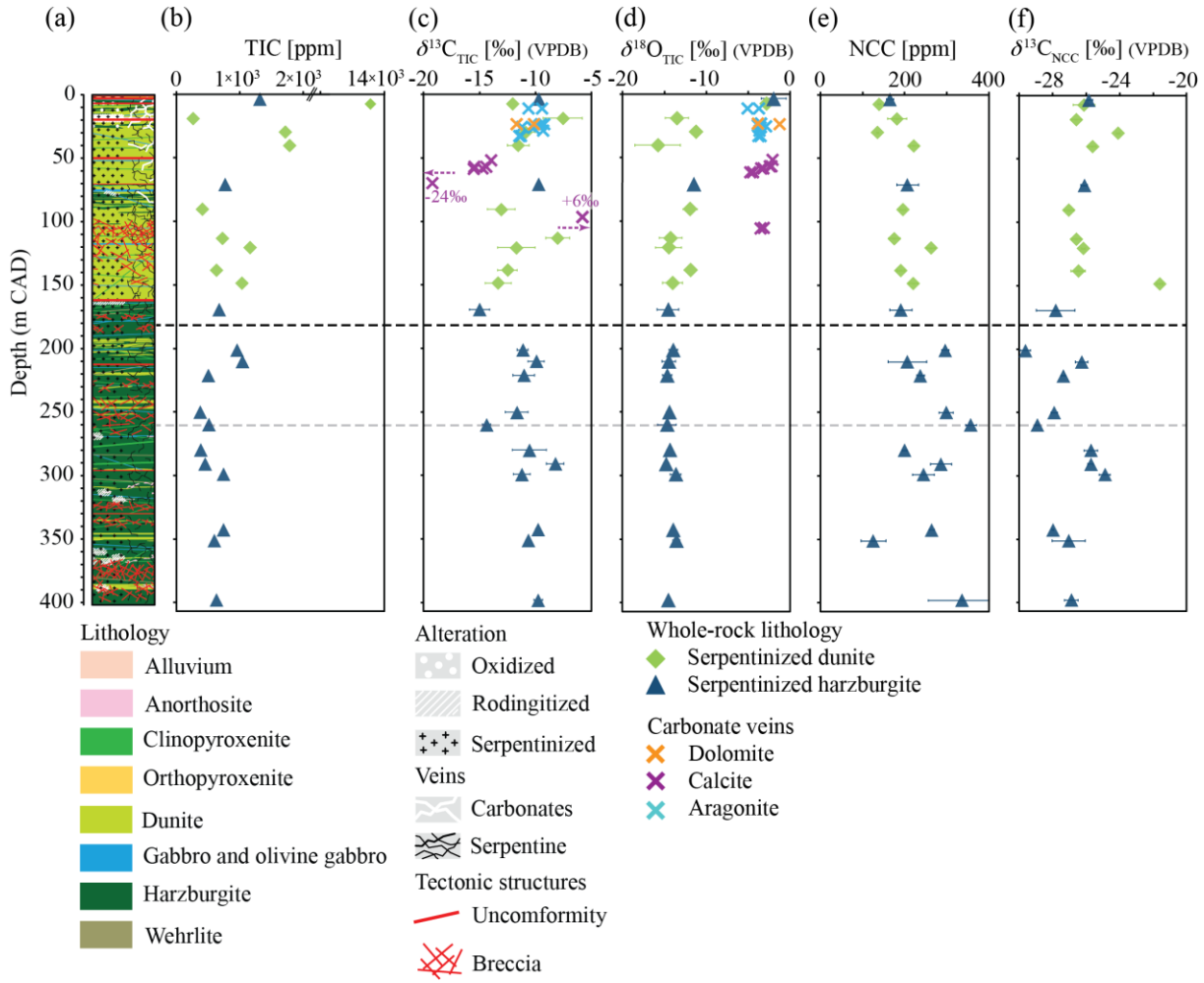

Figure 4. (a) Lithological profile of Hole BA1B, detailed information in Fig. 3 (modified after Kelemen, Matter, Teagle, et al., 2020). Variations in (b) total inorganic carbon (TIC) content, (c) $\delta^{13}C_{TIC}$ values, (d) $\delta^{18}O_{TIC}$ values (e) total non-carbonate carbon (NCC) content, and (f) $\delta^{13}C_{NCC}$ values with Chikyu Adjusted Depth (CAD) from serpentinized dunite and harzburgite whole-rock samples and carbonate veins from the Wadi Tayin Massif. Carbon isotope composition of four calcite veins plot outside Figure 3c, two samples show more ^{13}C depleted values and two are more ^{13}C enriched. Data are given in Table 2.

Samples from Hole BA1B have slightly less TC than Hole BA3A, with an average concentration of ~786 ppm and higher concentrations observed in the upper 40 m. $\delta^{13}C_{TC}$ values

of Hole BA1B range from -15.9 to -7.2 ‰. TC contents in serpentinites from Hole BA3A are homogenous and have an average value of ~1065 ppm, with one outlier with less than 700 ppm TC (~200 m). The $\delta^{13}C_{TC}$ values in Hole BA3A have a smaller range as in BA1B and lie between -9.5 to -5.8 ‰.

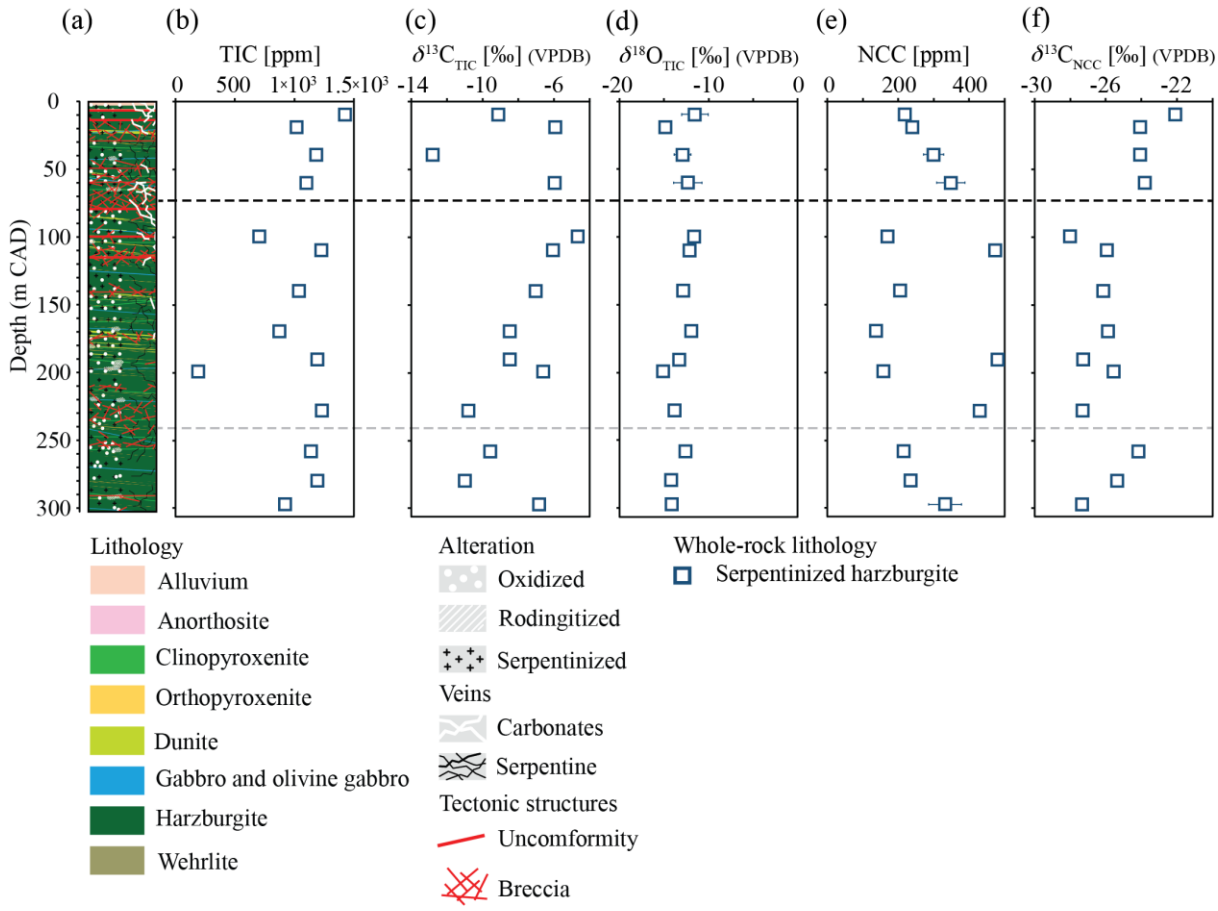

Figure 5. (a) Lithological profile of Hole BA3A, detailed information in Fig. 3 (modified after Kelemen, Matter, Teagle, et al., 2020). Variations in (b) total inorganic carbon (TIC) content, (c) $\delta^{13}C_{TIC}$ values, (d) $\delta^{18}O_{TIC}$ values (e) total non-carbonate carbon (NCC) content, and (f) $\delta^{13}C_{NCC}$ values with Chikyu Adjusted Depth from serpentinized harzburgite whole-rock samples from the Wadi Tayin Massif at the Samail Ophiolite.

Table 2. Carbon and oxygen isotope composition (VPDB), carbonate clumped isotope compositions, estimated formation temperature, and fluid equilibrium oxygen isotope compositions (VSMOW) of carbonate veins in ultramafic rocks from the Wadi Tayin Massif at the Samail Ophiolites.

Site	Hole	Core	Section	Interval (cm)		Depth (m CAD)		Lithology	Mineral		$\delta^{13}C_{TIC}$		$\delta^{18}O_{TIC}$		Δ47		T		$\delta^{18}O_{Fluid}$ [b]
				top	bot.	top	bot.			n	(‰)	σ	(‰)	σ	(‰)	σ	(°C)	68% CL[a]	(‰)
BA	1B	4	4	12	17	11.15	11.20	Serpentinized harzburgite	Aragonite	9	-10.61	0.02	-3.74	0.05	0.646	0.041	34	5	-0.40
BA	1B	4	4	12	17	11.15	11.20	Serpentinized harzburgite	Aragonite	9	-9.38	0.02	-5.12	0.06	0.639	0.023	36	3	-1.47
BA	1B	8	4	34	35	23.28	23.29	Serpentinized dunite	Aragonite	8	-9.48	0.03	-3.47	0.06	0.659	0.009	29	1	-1.09
BA	1B	8	4	34	35	23.28	23.29	Serpentinized dunite	Aragonite	9	-9.21	0.03	-3.55	0.04	0.662	0.020	28	2	-1.29
BA	1B	14	1	59	62	23.29	23.32	Serpentinized dunite	Dolomite	8	-11.70	0.03	-1.29	0.10	0.617	0.016	29	2	-1.34
BA	1B	8	4	61	66	23.55	23.60	Serpentinized dunite	Dolomite	9	-10.13	0.06	-3.85	0.06	0.580	0.047	43	7	-1.03
BA	1B	14	3	0	20	24.58	24.78	Serpentinized dunite	Aragonite	9	-9.64	0.05	-3.90	0.07	0.665	0.024	27	3	-1.81
BA	1B	14	3	81	84	25.39	25.42	Serpentinized dunite	Aragonite	8	-11.20	0.04	-2.92	0.04	0.664	0.023	28	3	-0.79
BA	1B	9	4	19	20	26.28	26.29	Serpentinized dunite	Aragonite	10	-10.17	0.02	-3.53	0.04	0.662	0.030	28	3	-1.24
BA	1B	10	3	4	6	28.66	28.68	Serpentinized dunite	Aragonite	8	-9.32	0.04	-3.66	0.08	0.630	0.031	39	4	0.61
BA	1B	17	1	17	22	32.87	32.92	Gabbro	Aragonite	10	-11.46	0.11	-3.79	0.13	0.670	0.012	26	1	-2.03
BA	1B	17	1	17	22	32.87	32.92	Gabbro	Aragonite	7	-11.27	0.01	-3.55	0.05	0.648	0.025	33	3	-0.44
BA	1B	25	2	8	16	51.68	51.76	Serpentinized dunite	Calcite	10	-13.94	0.01	-2.15	0.03	0.660	0.033	29	3	0.80
BA	1B	26	4	84	89	56.79	56.84	Serpentinized dunite	Calcite	9	-15.46	0.02	-2.27	0.03	0.650	0.039	32	4	1.29
BA	1B	26	4	79	83	56.74	56.78	Serpentinized dunite	Calcite	11	-14.42	0.01	-2.45	0.03	0.657	0.038	30	4	0.68
BA	1B	27	2	78	81	58.38	58.41	Serpentinized dunite	Calcite	11	-14.75	0.02	-3.50	0.04	0.657	0.024	30	2	-0.43
BA	1B	27	3	13	17	58.62	58.66	Serpentinized dunite	Calcite	12	-15.49	0.03	-3.26	0.08	0.664	0.030	28	3	-0.63
BA	1B	28	2	77	82	61.38	61.43	Serpentinized dunite	Calcite	9	-23.18	0.30	-4.49	0.06	0.634	0.016	37	2	-0.06
BA	1B	28	2	68	72	61.29	61.33	Serpentinized dunite	Calcite	8	-23.99	0.07	-4.77	0.02	0.656	0.016	30	2	-1.69
BA	1B	43	1	33	41	105.03	105.11	Olivine Gabbro	Calcite	7	4.44	0.06	-3.20	0.03	0.644	0.025	34	3	0.66
BA	1B	43	2	29	31	105.80	105.82	Serpentinized dunite	Calcite	9	6.87	0.12	-3.53	0.02	0.631	0.036	39	4	1.22

[n] number of replicate measurements; [a] Confidence Level (CL); [b] Calculated oxygen isotope compositions of the fluids

The serpentinized peridotites have a wide range of TIC contents, varying from 191 ppm to 1.4 wt%, with $\delta^{13}C_{TIC}$ values from -15.0 to -4.7 ‰ (Figures 4b - c, and 5b - c). The majority of the rocks from Hole BA1B have TIC contents around ~798 ppm, except for one sample from the uppermost oxidized section of the core with 1.4 wt%. The isotopic compositions of TIC in Hole BA1B range between -15.0 and -7.6 ‰, which is slightly more ^{13}C depleted than in BA3A. The dunite samples close to the dunite-harzburgite boundary show the most ^{13}C-depleted values with -13.4 ‰ within the dunitic sequence (Figure 4c). The harzburgites scatter around an average value of -10.9 ‰ and also show the most ^{13}C-depleted values close to the dunite-harzburgite boundary (Figure 4c). The harzburgites from Hole BA3A have homogenous TIC content ranging from 703 ppm to 0.1 wt%, with one outlier with less than 700 ppm (at ~200 m). The $\delta^{13}C_{TIC}$ values vary between -12.8 and -4.7 ‰ and generally decrease with increasing depth from 100 to 280 m (-4.7 to -11‰, Figure 5c).

The non-carbonate carbon concentrations in both cores are low and range from 126 to 479 ppm, with $\delta^{13}C$ values ranging from -29.6 to -21.6 ‰, typical of organic carbon fractions measured previously in oceanic serpentinites (Früh-Green et al., 2004; Delacour et al., 2008; Schwarzenbach et al., 2013) (Figures 4e - f, Figures 5e - f). In Hole BA1B, NCC content is around ~220 ppm and shows slightly more variation, higher concentrations, and overall lower $\delta^{13}C_{NCC}$ values in the harzburgite sequence in the lower part of the hole. $\delta^{13}C_{NCC}$ in Hole BA1B ranges from -29.6 to -24.1 ‰, with one outlier at -19.5 ‰ (Figure 4f). The serpentinized harzburgites from BA3A have the highest NCC concentrations and show an increase in NCC with depth in the first 100 m. Below this depth, there is a distinct bimodal distribution with peaks at ~190 and ~460 ppm, whereby the peak at approximately 190 ppm overlaps with the average NCC content in Hole BA1B (Figure 5e). A difference in $\delta^{13}C_{NCC}$ is also seen between the top 100 m, with $\delta^{13}C$ of ~ -23.5 ‰, and the deeper section with $\delta^{13}C$ of ~ -26.3 ‰ (Figure 5f). However, no distinct bimodal distribution compared to the NCC content at this depth interval is observed.

Table 3. Radiocarbon ages of carbonate veins and bulk rock samples from the Wadi Tayin Massif at the Samail Ophiolite.

Site	Hole	Core	Section	Interval (cm)		Depth (m CAD)		Lithology	Mineralogy	Sample type	Carbon type	$F^{14}C$		^{14}C ages	
				top	bot.	top	bot.						σ (%)	(yr)	σ
BA	1B	3	2	73	85	7.34	7.50	Serpentinized dunite	-	whole rock	inorganic	0.025	0.001	29750	321
BA	1B	3	2	73	85	7.34	7.50	Serpentinized dunite	-	whole rock	non-carbonate	0.185	0.002	13574	101
BA	1B	8	4	34	35	23.28	23.29	Serpentinized dunite	Aragonite	vein	inorganic	0.002	25.104	50464	2017
BA	1B	8	4	61	66	23.55	23.60	Serpentinized dunite	Dolomite	vein	inorganic	0.007	9.268	39886	745
BA	1B	20	3	0	50	40.10	40.60	Serpentinized dunite	-	whole rock	inorganic	0.878	0.006	1048	55
BA	1B	20	3	0	50	40.10	40.60	Serpentinized dunite	-	whole rock	non-carbonate	0.328	0.003	8966	83
BA	1B	26	4	79	83	56.74	56.78	Serpentinized dunite	Calcite	vein	inorganic	0.009	6.899	37464	554
BA	1B	28	2	68	72	61.29	61.33	Serpentinized dunite	Calcite	vein	inorganic	0.022	4.296	30811	345
BA	1B	43	1	33	41	105.03	105.11	Olivine gabbro	Calcite	vein	inorganic	0.005	10.610	42386	852
BA	1B	94	4	0	53	259.99	260.50	Serpentinized harzburgite	-	whole rock	inorganic	0.964	0.006	293	53
BA	1B	94	4	0	53	259.99	260.50	Serpentinized harzburgite	-	whole rock	non-carbonate	0.711	0.005	2738	56
BA	3A	27	1	28	88	60.00	60.60	Serpentinized harzburgite	-	whole rock	inorganic	0.908	0.006	771	56
BA	3A	27	1	28	88	60.00	60.60	Serpentinized harzburgite	-	whole rock	non-carbonate	0.337	0.003	8741	75
BA	3A	76	3	0	50	190.40	190.90	Serpentinized harzburgite	-	whole rock	inorganic	0.927	0.006	608	55
BA	3A	76	3	0	50	190.40	190.90	Serpentinized harzburgite	-	whole rock	non-carbonate	0.273	0.003	10440	76
BA	3A	106	2	0	50	279.60	280.10	Serpentinized harzburgite	-	whole rock	inorganic	0.915	0.007	717	63
BA	3A	106	2	0	50	279.60	280.10	Serpentinized harzburgite	-	whole rock	non-carbonate	0.366	0.005	8083	115

438

439 4.2.2 Carbon Isotope Geochemistry of the Veins

440 Carbon isotope compositions of the veins are given in Table 2. Dolomite (n = 2) and
441 aragonite (n = 10) were only found in the shallow part of Hole BA1B, and their $\delta^{13}C$ lie in a narrow
442 range from -11.7 to -9.2 ‰. The calcite veins (n= 9) can be divided into three distinct groups with
443 depth (Figure 4c). The deepest calcites at 105 m have ^{13}C-enriched values of ~ +5.7 ‰, calcites at
444 61 m have highly ^{13}C-depleted values of ~ -23.6 ‰, and the shallowest calcites at 56 m lie in a
445 narrow range from -15.5 to -13.9 ‰.

446 4.3 Radiocarbon Dating

447 Five carbonate veins and the inorganic and non-carbonate carbon of six whole-rock
448 samples show ^{14}C ages from 50,464 to 293 yr (Table 3, Figure 6). Carbonate veins yield ^{14}C ages
449 ranging from 50,464 to 30,811 yr. Because the veins often consist of multiple carbonate
450 generations, ^{14}C values can represent a mixed-age rather than a single precipitation phase. The
451 dolomite vein formed 39,886 yrs ago, and calcites ages range from 42,386 to 30,811 yr (Figure 6).
452 The aragonite vein has the oldest ^{14}C age with 50,464 yr.

453 The whole-rock samples have much younger formation ages and show a distinct variation
454 between the boreholes. In Hole BA1B, ^{14}C values of TIC decrease from 29,750 yr in the first 10
455 m to 293 yr at ~260 m depth, whereby the oldest age of whole-rock TIC (29,750 yr) coincides with
456 the latest carbonate vein formation with 30,811 yr (Table 3). In general, NCC in Hole BA1B
457 displays older ^{14}C ages than the TIC, except for a shallow sample in the first 10 m. Like TIC, ^{14}C
458 ages of the non-carbonate carbon progressively decrease with increasing depth from 13,574 to
459 2738 yr (Table 3). The inorganic and non-carbonate carbon from Hole BA3A are more
460 homogenous and yield ^{14}C ages of ~699 and ~9088 yr, respectively.

461 4.4 Oxygen Isotopes

462 The overall bulk rock oxygen isotope composition of dispersed carbonate is relatively
463 homogenous, with variations only seen in in the top 10 m of Hole BA1B, where two samples have
464 a $\delta^{18}O_{TIC}$ of -2.8 and -2.0 ‰ (VPDB) (Figures 4d); below this depth in Hole BA1B $\delta^{18}O_{TIC}$ lies in
465 a narrow range between -15.8 to -11.3 ‰. Variability is slightly higher in the serpentinized dunites.
466 The $\delta^{18}O_{TIC}$ of the bulk rocks from Hole BA3A lie in a similar and narrow range from -15.1 to -

11.5 ‰ as in Hole BA1B (Figures 5d). Erosion and replacement of the first couple of meters with alluvium may have removed the shallow more ^{18}O-enriched carbonates at Hole BA3A.

The δ^{18}O of the veins in Hole BA1B vary from -5.1 to -1.3 ‰ (Figures 4d and 6), similar to the δ^{18}O of the bulk samples of the first 10 m. Dolomites have δ^{18}O values from -3.9 to -1.3 ‰, calcites from -4.8 to -2.2 ‰, and aragonites show uniform δ^{18}O values within a narrow range of -3.9 to -3.5 ‰, with one outlier at -5.1 ‰.

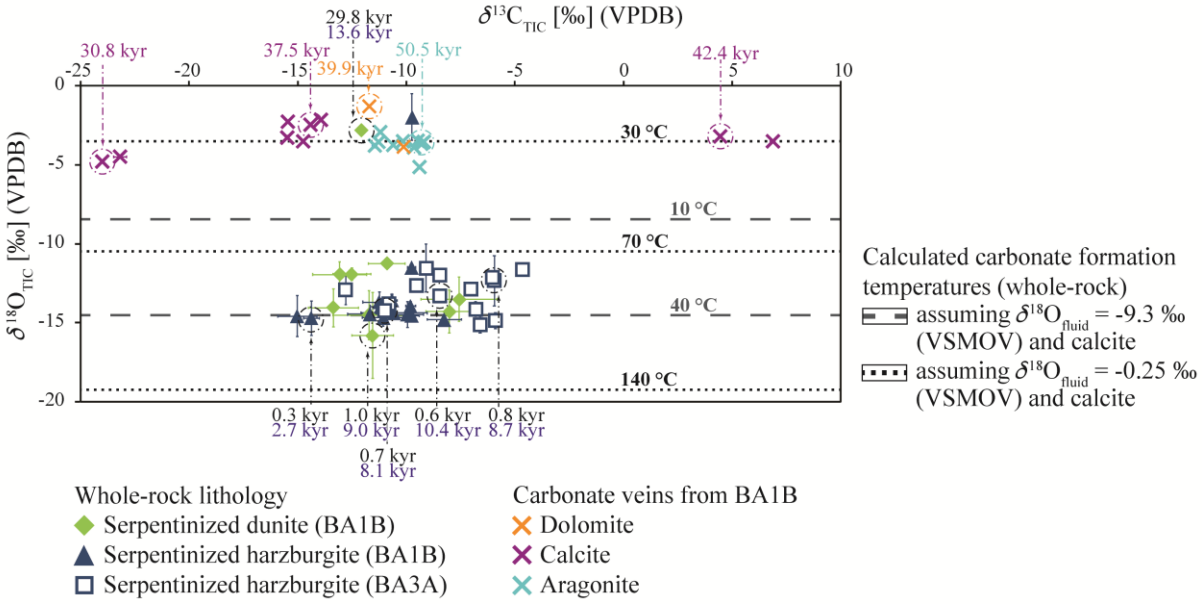

Figure 6. $\delta^{13}C_{TIC}$ versus $\delta^{18}O_{TIC}$ values of carbonate in serpentinized dunite and harzburgite from Hole BA1B and BA3A from the Wadi Tayin Massif of the Samail Ophiolite. Whole-rock samples are compared with isotope values of calcite, aragonite, and dolomite veins from Hole BA1B. ^{14}C ages are given for five veins (color-coded according to carbonate phases) and six bulk rock samples distinguishing total inorganic carbon (black number) and total non-carbonate carbon (blue). Estimated temperatures are shown as dashed and dotted lines using average modern ground- and meteoric water $\delta^{18}O_{Fluid}$ of -0.25 ‰ and the average calculated $\delta^{18}O_{Fluid}$ of -9.3 ‰, which would have been necessary for carbonate formation temperature of ~35 °C for the dispersed carbonates.

485 ## 4.5 Carbonate Precipitation Temperatures

486 ### 4.5.1. Oxygen Isotope Thermometry of TIC in Whole Rock Samples

487 Because of the low carbonate concentrations, it was not possible to measure clumped
488 isotopes of the bulk dispersed carbonate. Carbonate formation temperatures were thus estimated
489 using the oxygen isotope fractionation equation for calcite of O'Neil et al. (1969) corrected with
490 Friedman & O'Neil (1977) and the equation of Müller et al. (2019) for dolomite. As radiocarbon
491 dating indicates a recent formation age of these carbonates, to calculate $\delta^{18}O_{Fluid}$, we used the
492 two endmembers of -3.0 ‰ and +2.5 ‰ (VSMOW) measured on modern groundwater and
493 alkaline springs in the Samail Ophiolite as reported by Falk et al. (2016), Miller et al. (2016), and
494 Nothaft et al. (2020). Temperature estimates with $\delta^{18}O_{Fluid}$ = -3.0 ‰ result in lower values. The
495 calculated temperatures of formation range from 9 to 133 °C, assuming that all carbonates are
496 calcite, and from 30 to 204 °C, assuming they are dolomite. The TIC concentration in whole-
497 rock samples is below the detection limit of XRD, which limits identification of the predominant
498 carbonate phase. Due to the lack of dolomite and aragonite veins below 33 m and the measured
499 Type II fluid in deeper parts of wells at the Samail Ophiolite (Kelemen, Matter, Teagle, et al.,
500 2020), we assume that calcite is the main carbonate phase in the bulk rock samples.

501 The carbonates in the two shallow samples from Hole BA1B formed between 9 and 40 °C
502 (Table 1), which is consistent with the mean modern recharge temperature at shallow depth (< 50
503 m) of ~32 °C (Paukert Vankeuren et al., 2019). Dispersed carbonates below 10 m at Hole BA1B
504 consistently have higher calculated temperatures between 57 and 133 °C with no downhole trend.
505 In Hole BA3A, dispersed carbonates exhibit a similar temperature range as in Hole BA1B with
506 values from 59 to 127 °C (Figure 6). These calculated formation temperatures are unrealistic high,
507 considering the relative young formation ages of less than 1000 ^{14}C yrs. Therefore, we have to
508 assume that an ^{18}O-depleted fluid or disequilibrium processes rather than high formation
509 temperatures cause the ^{18}O-depleted signatures of the dispersed carbonates. Assuming a mean
510 modern recharge temperature of 35 °C and using the oxygen isotope fractionation equation of
511 O'Neil et al. (1969) corrected with Friedman & O'Neil (1977), the estimated $\delta^{18}O_{Fluid}$ range from
512 -11.5 to -7.0 ‰ (avg. -9.3 ‰, Figure 6).

513 4.5.2 Clumped Isotope Temperatures of Carbonate Veins

514 Clumped isotope temperatures vary from 26 to 43 °C (Table 2), which are in the range of
515 the ^{18}O-based temperatures of shallow bulk rocks of Hole BA1B. Dolomites have clumped isotope
516 temperatures of $T_{\Delta 47}$ = 29 to 43 °C. The calcites show $T_{\Delta 47}$ of 28 to 39 °C, and the aragonite veins
517 yield $T_{\Delta 47}$ of 26 to 39 °C. Calculated oxygen isotope values of the fluid in equilibrium with the
518 carbonates are ~ 0 ‰ ± 2 ‰. Fluids in equilibrium with dolomite veins have a restricted range of
519 -1.3 to -1.0 ‰, whereas fluids forming the calcite veins have more variable values from -1.7 to
520 +1.3 ‰, with no distinction between different depths. Similarly, the δ^{18}O of the fluids that
521 precipitated aragonites lie in a range of -1.8 to +0.6 ‰.

522 **5 Discussion**

523 Our observations and data suggest that the studied rocks in the Wadi Tayin Massif were
524 affected by two distinct phases of carbonate formation during the last 50 kyr (or longer): (i)
525 carbonate vein formation during focused fluid flow, at temperatures between 26 to 43 °C, from 30
526 kyr to over 50 kyr before present, which is limited to the dunitic sequence of BA1B and with
527 variable DIC sources. (ii) Pervasive disperse carbonization precipitated from an ^{18}O-depleted fluid
528 at moderate temperatures, with ^{13}C-depleted carbon likely derived from the respiration of OM.
529 Scicchitano et al. (2020) reported different stages of serpentinization and provided evidence for
530 early seafloor hydration and alteration from samples of Hole BA1B. Similarly, Noël et al. (2018)
531 suggest seawater derived-fluids leading to the earliest carbonate formation in samples from Wadi
532 Dima, Wadi Tayin Massif, north-west of the OmanDP Site BA. However, our study found no
533 evidence for carbonate formation during the oceanic phase of serpentinization of the Samail
534 Ophiolite. In the following, we discuss the evolution of carbonate formation in the Wadi Tayin
535 Massif and then discuss the implications for organic carbon storage in ultramafic rocks.

536 5.1 Carbonate Vein Precipitation and Focused Fluid Flow

537 Macroscopic brecciation and veining of the peridotite indicate that hydration and
538 carbonization were facilitated by deformation. The infiltration of fluids was likely controlled by
539 continuous fracture planes and micro-fracturing caused by serpentinization, forming permeability
540 pathways and channeling the fluids along specific domains of the mesh-textured peridotite. We
541 argue that focused fluid flow leads to the formation of carbonate veins in the more permeable

dunitic sequence of Site BA, with $T_{\Delta 47}$ indicating precipitation temperatures of 26 to 43 °C (Table 2).

The clumped isotope temperatures of Hole BA1B carbonate veins are in the same range as those previously reported for young carbonate veins (clumped isotope temperatures between 23 and 43 °C) formed during present-day weathering in the Samail Ophiolite (Streit et al., 2012). In addition, our data complement earlier thermometry estimates in the ophiolite that indicated slightly higher oxygen isotope-based temperatures of 20 to 60 °C for calcite veins in peridotite from outcrops and roadcuts with ^{14}C ages from 8 kyr to > 50 kyr (Kelemen et al., 2011; Mervine et al., 2014) and clumped and oxygen isotope temperatures between ambient and 60 °C for modern to > 45 kyr old travertine (Clark et al., 1992; Falk et al., 2016; Kelemen et al., 2011; Mervine et al., 2014). Our ^{14}C data suggest that the formation of the carbonate veins and the TIC of two shallow samples, with high amounts of veins, ranged from 30 kyr to > 50 kyr.

While the overall range of carbonate formation temperatures is similar to carbonates sampled in outcrops, their ages are restricted to a shorter period of time. We propose that low-temperature alteration by focused fluid flow was predominant in the shallow dunitic sequence and changed over time to pervasive alteration without the formation of carbonate veins below the present-day surface. However, as previously observed by Noël et al. (2018), carbonate veins can represent multiple phases of formation. Thus, the ^{14}C values can also represent a mixture of ages > 50 kyr and modern carbonates and would be consistent with previously reported ages of carbonates within peridotites at the Samail Ophiolite. Carbonates from listvenite and the metamorphic sole formed at much higher temperatures (clumped isotope temperatures between 52 and 247 °C, (Beinlich, Plümper, et al., 2020; Falk & Kelemen, 2015) during the Cretaceous and are related to different processes.

The range in $\delta^{13}C$ of -24.0 to +6.9 ‰ of the carbonate veins of Hole BA1B only partly overlaps with that reported for outcrops of the Samail Ophiolite (Figure 7a). In the uppermost 33 m, aragonite and dolomite veins lie in a similar but slightly more ^{13}C-depleted range. Deeper calcite veins only overlap with a single measurement from Noël et al. (2018). The comparison with literature data from different ophiolites worldwide (Figure 7b) shows a similar pattern, whereby the carbonate veins from the top 60 m of Hole BA1B coincide with previously reported values, including the shallower calcite veins. The higher variability in $\delta^{18}O$ reflects the variability of the

oxygen isotope composition of meteoric waters with latitude, distance from the vapor source, and amount of rainout (Rozanski et al., 1993) which explains the more enriched values at Oman.

The generally negative carbon isotope composition of the carbonates suggests a contribution from ^{13}C-depleted carbon likely derived from biologically mediated respiration of organic matter. Two veins show an elevated $\delta^{13}C$ (Figure 7a) which we attribute to a contribution of carbon from methanogenesis. A range of $\delta^{13}C$ from -15 to -8 ‰ in carbonates in Oman has previously been attributed to the respiration of organic matter in soils (Clark et al., 1992), which is a similar range as that measured in dolomite, aragonite, and in most of the calcite veins. These values represent a mixture of ^{13}C-depleted carbon from organic matter respiration, atmospheric CO_2 ($\delta^{13}C$ = ~ -7 ‰, Clark et al., 1992) and possibly bicarbonate from the dissolution of limestones. These carbon isotope compositions of the veins are in the same range as those of the DIC in Type I fluids (Mg^{2+} - HCO_3^-) in several wells in the Wadi Tayin Massif (-13.9 to -10.9 ‰, Nothaft et al., 2020).

Biological mediated respiration of OM can occur *ex-situ*, and ^{13}C- depleted carbon can be transported via the percolating fluid to the system and *in-situ* by organisms inhabiting the ultramafic rocks. Recent microbiological and metagenomic studies showed that microbial life can be sustained within the lithosphere and that microbial utilization of H_2, CH_4, and formate may be common in different serpentinization systems (Brazelton et al., 2012; Curtis et al., 2013; Daae et al., 2013; Etiope & Sherwood Lollar, 2013; Lang et al., 2018; Ohara et al., 2012; Schrenk et al., 2013). Recent rRNA and lipid biomarker analyses of carbonate veins, travertine, and altered peridotites from the Samail Ophiolite provided evidence for the existence of a common core serpentinization microbiome (Newman et al., 2020). This microbiome has been previously described at the submarine, serpentine-hosted Lost City hydrothermal field (LCHF) (Bradley et al., 2009; Lincoln et al., 2013; Méhay et al., 2013). Specifically, microorganisms include sulfate-reducing and ammonia-oxidizing bacteria, methanogens, and methanotrophs. Therefore, it is possible that biologically mediated respiration of OM within the basement mixed with atmospheric CO_2 dissolved in the meteoric waters could be the predominant carbon sources for the carbonate veins.

602

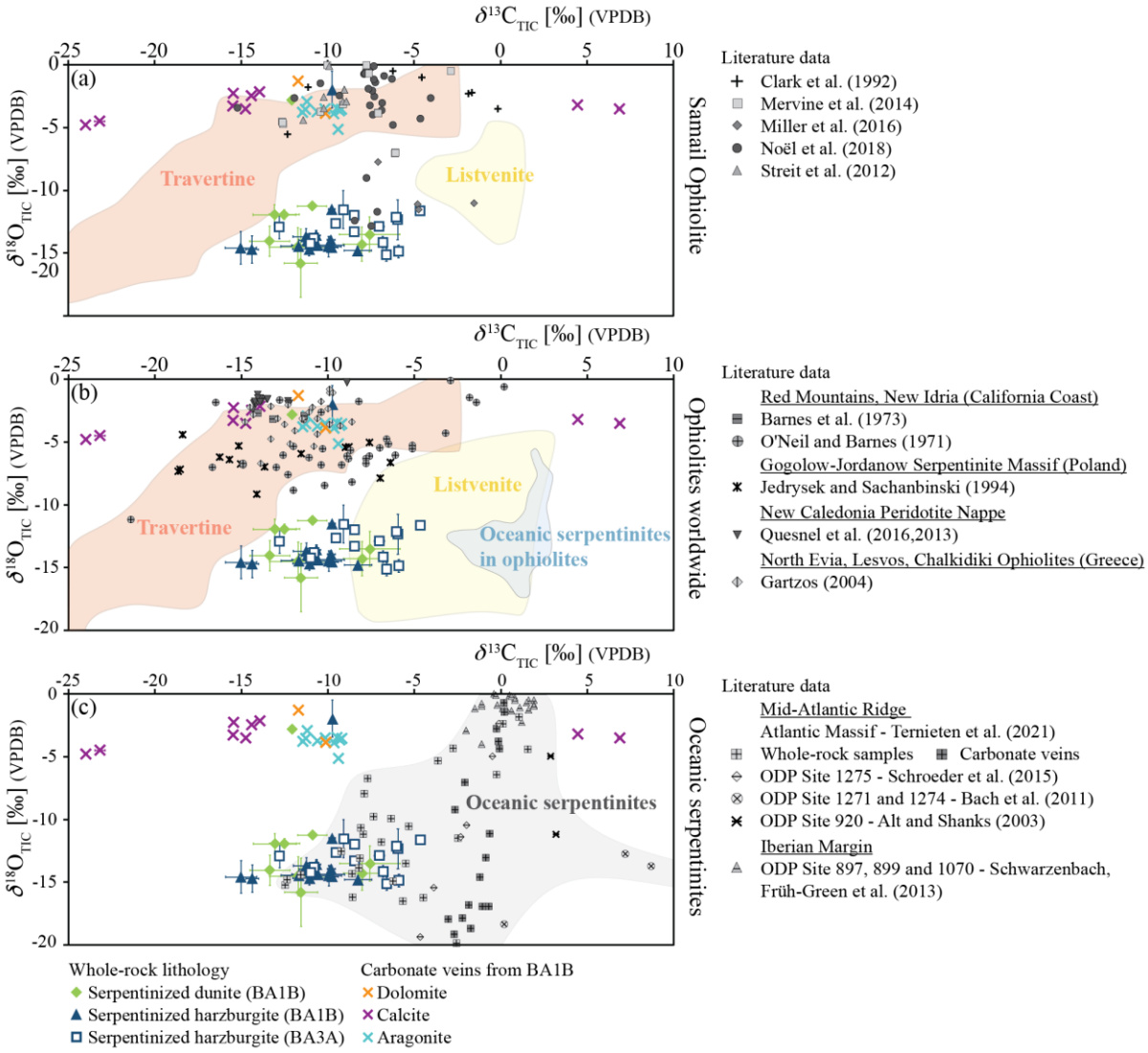

603

604 **Figure 7.** Whole-rock $\delta^{13}C_{TIC}$ values versus $\delta^{18}O_{TIC}$ of serpentinized peridotites from Hole
605 BA1B and BA3A, plotted together with isotope values of calcite, aragonite, and dolomite veins
606 from Hole BA1B from the Wadi Tayin Massif. Isotopic compositions of carbonates of this study
607 are compared with results from previous studies on samples from (a) the Samail Ophiolite, (b)
608 ophiolites worldwide, and (c) oceanic serpentinite. (a) The range from listvenites (Beinlich,
609 Plümper, et al., 2020; Falk & Kelemen, 2015) and travertine/carbonate crusts from alkaline
610 springs (Clark et al., 1992; Falk et al., 2016; Mervine et al., 2014) are marked as yellow and
611 orange fields, respectively, and data of carbonate veins within serpentinized peridotites from

612 Clark et al. (1992), Mervine et al. (2014), Miller et al. (2016), Noël et al. (2018), and Streit et al.
613 (2012) are plotted. (b) The range from listvenites is indicated by a yellow field and is defined by
614 values from Fig. 7a and additional from the Appalachians and Advocate Listvenite in Canada
615 (Auclair et al., 1993; Menzel et al., 2018), Linnajavri and Leka Ophiolite in Norway (Beinlich et
616 al., 2012; Bjerga et al., 2015), and the Birjand Ophiolite in Iran (Boskabadi et al., 2020). The
617 range for oceanic serpentinites is defined by values from the Northern Apennine ophiolites in
618 Italy (Schwarzenbach, Früh-Green, et al., 2013) and for travertine deposits by values from Fig.
619 7a, the Voltri Massif and different deposits in California (O'Neil & Barnes, 1971;
620 Schwarzenbach, Lang, et al., 2013), indicated by blue and orange fields, respectively. Values
621 from carbonate veins are plotted from the Red Mountains and New Idria in California (Barnes et
622 al., 1973; O'Neil & Barnes, 1971), Gogolow-Jordanow serpentinite massif in Poland (Jedrysek
623 & Sachanbinski, 1994), from the New Caledonia peridotite nappe in New Caledonia (Quesnel et
624 al., 2013, 2016) and various ophiolites located in Greece (Gartzos, 2004). (c) Isotopic
625 composition of sub-seafloor ultramafic hosted hydrothermal carbonates (Alt & Shanks, 2003;
626 Bach et al., 2011; Schroeder et al., 2015; Ternieten et al., 2021) and inorganic carbon from
627 oceanic serpentinites and gabbro-intruded impregnated ultramafic rocks from the Iberian Margin
628 and the Atlantis Massif (Schwarzenbach, Früh-Green, et al., 2013; Ternieten et al., 2021) are
629 shown.

630

631 The two calcite veins at about ~61 m depth have highly ^{13}C- depleted values ($\delta^{13}C$ = ~ -24
632 ‰, Figures 4c and 6), which may indicate a stronger influence of Type II fluids (Ca^{2+} - OH^-) that
633 have a reported DIC composition of -30 ‰ (NSHQ04, Nothaft et al., 2020), or a higher input of
634 ^{13}C-depleted inorganic carbon from anaerobic oxidation of methane. Nothaft et al. (2020) reported
635 16S rRNA data that showed the presence of microbes capable of CH_4 oxidation, which produces
636 highly ^{13}C-depleted inorganic carbon (e.g., Drake et al., 2015; Pedersen et al., 1997). Alternatively,
637 the more ^{13}C-depleted carbonate veins could also be explained by a Rayleigh distillation of the
638 DIC in the fluid caused by progressive carbonate precipitation. After removal of about 90 % DIC
639 with a $\delta^{13}C$ of -20 ‰ by carbonate precipitation with a fractionation factor between DIC and
640 calcite of 2 ‰ (i.e., with the calcite being 2 ‰ heavier than the DIC), the residual DIC in solution

reaches $\delta^{13}C$ of approximately -25 ‰. This residual DIC could result in precipitation of carbonates with $\delta^{13}C$ = ~-23 ‰, leading to the range we measure in the carbonate veins.

The two veins with strongly positive $\delta^{13}C$ can be related to methanogenic activity. Methanogenic archaea reduce CO_2 to methane leading to extreme isotopic enrichment of the residual DIC (Deppenmeier et al., 1996). Recent sequencing studies provided evidence for a widespread occurrence of the 16S rRNA gene affiliated with methanogens in well waters close to Site BA (Nothaft et al., 2020). However, both veins that show highly enriched ^{13}C compositions ($\delta^{13}C$ = ~ +6 ‰) are located below 100 m (BA1B), which in combination with highly alkaline conditions may limit the ability of micro-organisms to thrive in this environment, but does not exclude it. We propose that most of the ^{13}C-enriched DIC is transported with the percolating fluid and *in-situ* production only contributes to a minor amount.

Assuming that the carbonates were precipitated in isotopic equilibrium, we can calculate the $\delta^{18}O$ of the fluid using clumped isotope temperatures. Calculated $\delta^{18}O_{Fluid}$ lie in a range from -2 to +1.3 ‰ ± 2 ‰, overlapping previously reported values of -3.0 to +1.9 ‰ from modern ground- and well waters (Miller et al., 2016; Nothaft et al., 2020; Paukert Vankeuren et al., 2019). We propose that late post-obduction serpentinization leads to the formation of low-temperature carbonates caused by a fracture-controlled fluid circulation comparable to modern groundwater of Type I and Type II. Additionally, the carbonate mineralogy shows a distinction between shallow areas (top 33 m) with dolomite and aragonite and deeper areas (52 to 106 m) with calcite only, which is consistent with a change from an Mg^{2+}-rich Type I to a Ca^{2+}-rich and Mg^{2+}-poor Type II fluid at approximately 50 meters below the surface. Previous studies have proposed that Type I fluids mixed with DIC lead to the formation of magnesite and dolomite and Type II fluids exposed to the atmosphere to the precipitation of calcite (Barnes et al., 1967, 1978; Barnes & O'Neil, 1969; Bruni et al., 2002; Cipolli et al., 2004; Kelemen et al., 2011; Neal & Stanger, 1985; Paukert et al., 2012). In addition, previous geochemical and isotopic data of the Al Khwad fan in northern Oman also observed distinct aquifers: a deep aquifer below 300 m depth containing old groundwater; an intermediate aquifer between 50 and 300 m containing mixed groundwater; and a shallow aquifer filled with recently infiltrated groundwater (Weyhenmeyer et al., 2000, 2002).

The precipitation of low-temperature dolomite is still poorly understood. Previous studies showed that abiotic formation of dolomite at low temperatures is inhibited by slow reaction

kinetics (Sibley et al., 1987) caused by a lack of nucleation sites (Bosak & Newman, 2003), cation desolvation (Brady et al., 1996), sulfate inhibition (Baker & Kastner, 1981), and lack of solution supersaturation (Arvidson & Mackenzie, 1999). Microbial activity, however, has been shown to catalyze dolomite formation by sulfate reduction, methanogenesis, methanotrophy, sulfide oxidation, and aerobic respiration (Kenward et al., 2009; Moore et al., 2004; Moreira et al., 2004; Sánchez-Román et al., 2009; Vasconcelos et al., 1995). Newman et al. (2020) and Nothaft et al. (2020) reported rRNA gene sequences and lipid biomarker that suggest that sulfate-reducing bacteria, methanogens, and methanotrophs are widespread in the aquifer at the Wadi Tayin Massif. However, we propose that a high Mg/Ca ratio of a Type I groundwater (ranging between 7 and 66, Nothaft et al., 2020) possibly coupled with microbial activity leads to dolomite formation. More analyses of the influence of microbial activity in forming Mg-rich carbonate in these rocks are necessary to evaluate the potential effect of microbial metabolism on dolomite precipitation in ultramafic rocks.

5.2 Recent Dispersed Carbonate Precipitation

The influx of groundwater during later alteration of the peridotites occurs via a fine network along grain boundaries and micro-fractures, which leads to the formation of dispersed carbonates with progressive hydration of the entire Wadi Tayin Massif. Dispersed carbonates are the predominant carbonate occurrence and are not limited to specific lithology, depth, or cores, which suggest that pervasive fluid flow and alteration is the predominant carbonization mechanism at the Wadi Tayin Massif. ^{14}C ages between 1050 and 290 yrs indicate that dispersed carbonates precipitation is recent and thus that hydration and carbonization of the ultramafic rocks is an ongoing process. This is consistent with the presence of highly alkaline spring- and well waters, which demonstrate ongoing serpentinization in the Samail Ophiolite today (Kelemen et al., 2011; Kelemen & Matter, 2008; Neal & Stanger, 1985).

Dispersed carbonates have, similar to the carbonate veins, an isotope signature indicating a ^{13}C-depleted DIC source ($\delta^{13}C$ from -15.0 to -4.7 ‰, Figure 6) from biologically mediated respiration of OM mixed with atmospheric CO_2 (see section 5.1 for more details). The dispersed carbonates are characterized by variable $\delta^{13}C$ that show no correlation with TIC content, ^{14}C ages, and/or oxygen isotope composition. However, they show a distinct shift in composition before or after unconformities and highly brecciated zones at ~180 and ~206 m (BA1B) and ~70 m (BA3A)

(Figures 4c and 5c). This suggests that the percolating fluid is heterogeneous and with a variable contribution of biologically-derived carbon. Thus, we propose that fluid mixing is a common process at the Wadi Tayin Massif and that fluids can infiltrate the basement at different times and structural levels such as fracture planes, micro-fractures, and grain boundaries, causing highly heterogenous signatures controlled by tectonic features.

When assuming a modern groundwater oxygen isotope composition, calculated oxygen isotope temperatures of the dispersed carbonates range from 57 to 133 °C. These temperatures are unrealistically high, considering the relatively young formation ages, shallow depths, and lack of any apparent heat source. Paukert Vankeuren et al. (2019) estimated a mean modern recharge temperature of 32 °C at depths < 50 m in the peridotite aquifers of Oman. The highly ^{18}O-depleted compositions in carbonates can be either caused by (i) isotopic disequilibrium precipitation during rapid carbonate formation in the high pH fluids or by (ii) precipitation from a much more ^{18}O-depleted fluid than present-day groundwater.

(i) Clark & Fontes (1990) described a substantial depletion in ^{13}C and ^{18}O of travertines in the Samail Ophiolite during precipitation of carbonates caused by CO_2 uptake from the atmosphere and carbonate precipitation at the air-fluid interface under high pH condition. A strong kinetic isotope fractionation on the order of 19 to 24 ‰ at 25 °C occurs by the unidirectional reaction of $CO_{2(aq)}$ with OH^-, which are isotopically lighter than H_2O molecules (Zeebe, 2020), leading to strongly ^{18}O and ^{13}C depleted carbonates. Previous studies from Miura et al. (2011) provided evidence for the presence of H_2 and CH_4 together with H_2O in inclusions in olivine and orthopyroxene in harzburgites from the northern Samail Ophiolite. In addition, Nothaft et al. (2020) concluded that a higher amount of fluid inclusions are necessary to explain the isotopic signature of CH_4 in the well waters of Site BA. If our samples contained a higher amount of aqueous fluid inclusions, they might have reacted with atmospheric CO_2 during crushing and sample preparation, leading to carbonate precipitation with a highly depleted $\delta^{18}O$ composition. Thus, the ^{14}C ages (1050 to 290 yr) could represent a mixture of predominantly modern precipitated contamination and only a minor contribution of older carbonates formed during hydration of the Wadi Tayin Massif.

However, the carbon isotope signature is not as negative as commonly observed in carbonates precipitated from high pH fluids (Travertine range in Figures 7a and b) (Clark et al.,

1992; Falk et al., 2016; Mervine et al., 2014). Furthermore, previous analyses performed in the same laboratory (Geologisches Institute, ETH Zurich) on MBio-type samples recovered from the Atlantis Massif, Mid-Atlantic Ridge, addressing similar questions, have not reported conspicuous ^{18}O-depleted carbonates (Ternieten et al., 2021). Therefore, we conclude that contamination of carbonates during sample preparation is unlikely to explain the highly depleted ^{18}O carbonates or only contribute a negligible influence on the isotopic signal.

(ii) Another explanation is that the dispersed carbonates formed from a much more ^{18}O depleted fluid than present-day groundwater. Assuming calcite as the dominant carbonate phase and a mean formation temperature of 35 °C, the $\delta^{18}O$ of the percolating fluid would be between -11.5 to -9.3 ‰. Scicchitano et al. (2020) reported *in-situ* oxygen isotope analysis of serpentine minerals from Hole BA1B and proposed three serpentinization stages with fluids with distinct ^{18}O values. Their Stage II serpentinization by meteoric water that formed late banded chrysotile veins required a fluid with a $\delta^{18}O$ of ~ -7 ‰, much lower than modern groundwater. Other evidence of meteoric waters with more depleted $\delta^{18}O$ values are from speleothem fluid inclusions from the last interglacial period (~ 125 kyr), from a cave in northern Oman with $\delta^{18}O$ values of ~ -7.8 ‰ (Fleitmann et al., 2011; Nicholson et al., 2020). In addition, Streit et al. (2012) reported calculated $\delta^{18}O$ of the fluid in equilibrium with magnesite veins of -7.7 ‰.

These previous studies suggest that ^{18}O depleted fossil groundwaters are possible within the Samail Ophiolite and that the dispersed carbonates may have precipitated from a fluid that has led to late-stage serpentinization. Thus, the dispersed carbonates may represent a mixture of older and younger carbonates with fossil and modern ground and spring water components.

5.2.1 Dispersed Carbonates as Products of Deeper Fluid Circulation?

The carbon and oxygen isotope signatures of the dispersed carbonates are distinct from those of carbonate veins from our study and other localities in the Samail Ophiolite. Previous studies include carbonate veins in peridotites formed during present-day weathering (Mervine et al., 2014; Streit et al., 2012) from outcrop and drilled samples of listvenite and the metamorphic sole (Beinlich, Plümper et al., 2020; Falk & Kelemen, 2015), and travertines (Clark & Fontes, 1990; Falk et al., 2016, and reference therein) (Figure 7a). However, the dispersed carbonates in our study show similar compositions to the early dolomite veins from Noël et al. (2018) and matrix

carbonates from drill cuttings of the wells NSHQ04 and NSHQ14 at Site BA (Miller et al., 2016) (Figure 7a). The dolomite veins have been attributed to pervasive fluid flow at high-temperature conditions at the seafloor in the Jurassic (Noël et al., 2018). However, the radiocarbon ages of our samples exclude such an early formation for the dispersed carbonate at Site BA. The same observation is made by comparing the dispersed carbonates with carbonates from other ophiolites (Figure 7b). Dispersed carbonates have distinct compositions, except for listvenites from Newfoundland (Auclair et al., 1993), but they are similar to listvenites from the Samail Ophiolite, related to different chemical processes. The isotopic compositions of the investigated dispersed carbonate overlap with those formed during ocean-floor serpentinization at the Atlantis Massif (Figure 7c, $\delta^{13}C_{TIC}$ = -14 to -2 ‰; $\delta^{18}O_{TIC}$ = -17 to -6 ‰; Ternieten et al., 2021). However, the ^{14}C ages exclude an early ocean-floor serpentinization-related origin of the dispersed carbonates. These results provide evidence that radiocarbon analyses are essential for a correct interpretation of the origin of carbonates.

The results of our study suggest that dispersed carbonates precipitated from meteoric water and are enriched in ^{13}C- and ^{18}O- depleted bicarbonate due to potential mixing with deeper fossil groundwater. They occur throughout the entire Wadi Tayin Massif indicating large-scale hydration and represent the most recent carbonate formation, whereas older generations may have been dissolved. Serpentinized peridotites in outcrops and surface samples often contain high amounts of carbonate veins, which may overprint lower amounts of dispersed carbonates. This could explain the low number of previously reported carbonates with ^{13}C- and ^{18}O-depleted signatures at the Samail Ophiolite. We suggest that micro-fracturing caused by serpentinization provides the percolating fluid pathway and that they probably became one of the main natural hydraulic plumbing systems contributing to modern wadis and alkaline springs in the Samail Ophiolite. The occurrence of relatively young carbonates provides further evidence for the ongoing weathering and active serpentinization in the mantle section of the Samail Ophiolite. However, further investigations of the carbonate formation are necessary to understand the evolution from initial to recent carbonization.

5.4 Serpentinites as a Microbial Habitat and Sink for Organic Carbon?

Recent studies have shown that the ultramafic basement can sustain microbial life (Barry et al., 2019; Colman et al., 2017; Fullerton et al., 2019). The isotopic composition of carbonates in

our study shows that ^{13}C-depleted carbon is a significant contributor to carbonate precipitation in the system. Serpentinites from the wells NSHQ14 and NSHQ04 have very variable TOC concentrations of < 0.01 - 0.37 wt% (Miller et al., 2016), whereby the high values may be overestimated due to residual magnesite in the samples. The highest NCC content measured in our study is ~500 ppm, and both holes show distinct trends that can be correlated to unconformities, fractures, and heavily brecciated zones. Hole BA1B shows a shift to slightly higher NCC concentrations and lower $\delta^{13}C_{NCC}$ at the transition from dunites to harzburgites (Figures 4e and f). A similar change to more ^{13}C-depleted values can also be observed at Hole BA3A below the unconformity at ~80 m (Figure 5e). The total concentration at BA3A shows an increase in NCC with depth above the unconformity and only locally higher concentrations below.

We propose that the observed changes in the carbon isotope composition of NCC at unconformities and highly brecciated zones reflect changes in the hydrology of the system and that a higher fluid flow can lead to either removal or addition of organic carbon. The dunites have a higher permeability than the harzburgites (Katayama et al., 2020), potentially leading to higher fluid fluxes, which could have led to the removal of previously present NCC. This may also be true for the uppermost highly oxidized 10 m of BA3A that show a lower NCC content than deeper sections. Higher fluid flow is, in general, correlated to a potentially higher *in-situ* production due to more favorable nutrient cycling and, consequently, higher organic carbon contents. However, at Site BA, parts of the organic carbon may have been removed by the present-day percolating groundwater, oxidation and carbonate precipitation. The ^{14}C values of NCC suggest that the accumulation of the non-carbonate carbon occurred post-obduction between 14 kyr to 3 kyr, which is older than the dispersed carbonates. This would indicate an early emplacement and later removal of the non-carbonate carbon, possibly by the same pervasive fluid that leads to dispersed carbonate formation. Nevertheless, these ages are based on whole-rock investigations, and we have to consider that they represent a mixture of older and modern non-carbonate carbon.

The isotopic composition of NCC in the serpentinites from the Wadi Tayin Massif ($\delta^{13}C_{NCC}$ = -29.6 to -21.6 ‰) differ from the isotopic compositions of organic compounds previously analyzed in well waters from NSHQ04 and NSHQ14 at Site BA ($\delta^{13}C_{CH4,\ short\text{-}chain\ hydrocarbons}$ = -6.7 to +6.8 ‰, Nothaft et al., 2020). Nothaft et al. (2020) suggest a combination of mantle carbon leached from fluid inclusions and microbial activity of methanogens leads to the ^{13}C-enriched

compositions. In contrast, the isotopic composition of NCC from the Wadi Tayin Massif coincides with the $\delta^{13}C$ of oceanic NCC from serpentinized peridotites from the Atlantis Massif, host of the LCHF, which ranges from -28.3 to -19.8 ‰ (Ternieten et al., 2021). Additionally, recent rRNA and lipid biomarker analyses of carbonate veins, travertine, and altered peridotites from the Samail Ophiolite (Newman et al., 2020) provide evidence for the existence of a similar serpentinization microbiome compared to the one occupying the serpentine-hosted Lost City hydrothermal field (Bradley et al., 2009; Lincoln et al., 2013; Méhay et al., 2013). These results provide evidence supporting the hypothesis of a specific serpentine inhabiting community occurring in oceanic and continental environments. However, based on our results, we cannot distinguish whether microbial production of organic compounds occurs *in-situ* or whether they are transported via percolating fluids. In addition, fluid inclusions have been reported previously from the mantle peridotites of the Samail Ophiolite (Miura et al., 2011), and we have to consider leached CH_4 from inclusions as a potential contribution. However, the measurable ^{14}C ages of NCC indicate that mantle carbon only contributes to a minor amount.

To summarize, we suggest a mixture of microbial production combined with minor mantle carbon leached from volatiles and transported via the infiltrating fluid as the NCC source in the mantle rocks from the Wadi Tayin Massif. It is later removed in the shallow subsurface and dunitic sequence by more recent pervasive fluid flow, causing dispersed carbonate formation controlled by micro-fractures that may represent one of the main natural hydraulic plumbing systems within the Samail Ophiolite today.

5 Conclusions

Oman Drilling Project Holes BA1B and BA3A drilled through 400 and 300 m of serpentinized peridotite, respectively, containing several mafic intrusions, fractures, and unconformities. Carbonate occurrences show no record of initial ocean-floor hydration and serpentinization of the Samail Ophiolite. Clumped isotope thermometry of selected veins indicates a carbonation temperature range between 26 to 43 °C, which corresponds with mean modern recharge temperatures and post-obduction formation ages of the carbonates. The measured carbon and oxygen isotopes are in part similar to previously investigated carbonates from the Samail Ophiolite but also show distinct characteristics.

We argue that the available data are best explained by a model where focused fluids similar to modern ground- and meteoric water were locally channeled and reacted with the surrounding rock leading to the formation of calcite, dolomite, and aragonite veins in more permeable sections of the ophiolite from ~50 kyr to ~30 kyr. This first recorded phase of carbonization is followed by pervasive infiltrating fluids leading to dispersed carbonate precipitation within the entire Wadi Tayin Massif characterizing the large-scale hydration and alteration of the Samail Ophiolite from 30 kyr until at least 300 yr ago. Apparent correlations between heterogenous carbon isotopes of the dispersed carbonates and various tectonic features point to infiltration of the reactive fluids at different times and structural levels like fracture planes caused by deformation, micro-fractures from serpentinization, and grain boundaries. Such a model could also explain the highly ^{18}O-depleted composition of the dispersed carbonates. The pervasive nature of the later infiltrating fluid may lead to mixing with low amounts of fossil groundwater with δ^{18}O values of -7.8 ‰ (Nicholson et al., 2020). Proportions of mixing may be determined by the relative access that the percolating fluids have to fossil groundwater within the serpentinized peridotites.

These observations also show the importance of a multifaceted approach for creating a conceptual model for heterogeneous alteration and carbonization. Stable oxygen and carbon isotope investigations by themselves can be ambiguous, but including ^{14}C ages of even small amounts of carbon are essential for more realistic constraints on the system and can provide information about the impact of infiltrating fluids on the Semail Ophiolite. The observation of low amounts of recent carbonate precipitation provides no evidence for extensive fluid flow within the drilled 300 and 400 m, although highly alkaline properties of the well waters (Kelemen, Matter, Teagle, et al., 2020) indicate active serpentinization. This observation is relevant not only for the application of serpentinites as artificial CO_2 storage but also provides information about the potential for microorganisms to thrive within the ultramafic basement.

Our study suggests that post-obduction deformation facilitated repeated advective fluid infiltration into the ophiolite, followed by diffusive transport through the interconnected nano-scale serpentinite pore network that may represent one of the main present-day natural hydraulic plumbing systems within the Samail Ophiolite. Given the increasing appreciation of water-rock interactions in biological and economically important settings, insights into the carbon cycle may

878 aid in studies of the origin of life and the evaluation of the potential of mantle rocks to store carbon
879 and reduce CO_2 emission in the future.

880 **Acknowledgements**

881 We would like to thank Madalina Jaggi, Negar Haghipour, Stewart Bishop, and Lydia
882 Zehnder for help with sample preparation and analyses at ETH. This project was made possible
883 through funding by the International Continental Scientific Drilling Project (ICDP, lead PI's
884 Kelemen, Matter & Teagle), the Sloan Foundation – Deep Carbon Observatory (Grant 2014-3-01,
885 Kelemen PI), the National Science Foundation (NSF-EAR-1516300, Kelemen PI), the NASA
886 Astrobiology Institute (NNA15BB02A, Templeton PI), the German Research Foundation (DFG,
887 Koepke PI), the Japanese Society for the Promotion of Science (JSPS, 16H06347, Michibayashi
888 PI, and 19H00730, Morono PI), the European Research Council (Jamtveit PI), the Swiss National
889 Science Foundation (Früh-Green PI), the Japanese Marine Science and Technology Center
890 (JAMSTEC), the TAMU-JR Science operator, and in-kind contributions from the Sultanate of
891 Oman Ministry of Regional Municipalities and Water Resources, the Oman Public Authority of
892 Mining, Sultan Qaboos University, CRNS- Univ. Montpellier II, Columbia University, and the
893 University of Southampton, and through the efforts of the entire ICDP Expedition 5057 Oman
894 Drilling Project scientific party and support staff from the Oman Drilling Project Science Operator.
895 In particular, we thank Jude Coggon, Damon Teagle, and Mazin Al Sulaimani for all their logistical
896 support and Marguerite Goddard and Katsuyoshi Michibayashi for their leadership and in the BA
897 core characterization onboard D/V Chikyu.

898 We gratefully acknowledge funding by the Swiss National Science Foundation (SNF)
899 project No. 200021_163187 and subawards from the Deep Carbon Observatory No. 2019 G
900 VA217 to Früh-Green. Results of individual analyses of the samples will be available online on
901 PANGAEA (www.pangaea.de); however, the editorial process is still ongoing. In the meantime,
902 we attached the three data files that will be stored on PANGAEA as supplements to this
903 manuscript, precisely: Supplement 1 (the average analytical results of the stable isotope
904 measurements), Supplement 2 (replicate analyses of the clumped isotope measurements), and
905 Supplement 3 (average analytical results of the radiocarbon measurements).
906

References

Alt, J. C., & Shanks, W. C. (2003). Serpentinization of abyssal peridotites from the MARK area, Mid-Atlantic Ridge: Sulfur geochemistry and reaction modeling. Geochimica et Cosmochimica Acta, 67(4), 641–653. https://doi.org/10.1016/S0016-7037(02)01142-0

Arai, S., Ishimaru, S., & Mizukami, T. (2012). Methane and propane micro-inclusions in olivine in titanoclinohumite-bearing dunites from the Sanbagawa high-P metamorphic belt, Japan: Hydrocarbon activity in a subduction zone and Ti mobility. Earth and Planetary Science Letters, 353–354, 1–11. https://doi.org/10.1016/j.epsl.2012.07.043

Arvidson, R. S., & Mackenzie, F. T. (1999). The dolomite problem; control of precipitation kinetics by temperature and saturation state. *American Journal of Science*, *299*(4), 257–288. https://doi.org/10.2475/ajs.299.4.257

Auclair, M., Gauthier, M., Trottier, J., Jebrak, M., & Chartrand, F. (1993). Mineralogy, geochemistry, and paragenesis of the Eastern Metals serpentinite-associated Ni-Cu-Zn deposit, Quebec Appalachians. *Economic Geology*, *88*(1), 123–138. https://doi.org/10.2113/gsecongeo.88.1.123

Bach, W., Rosner, M., Jöns, N., Rausch, S., Robinson, L. F., Paulick, H., & Erzinger, J. (2011). Carbonate veins trace seawater circulation during exhumation and uplift of mantle rock: Results from ODP Leg 209. *Earth and Planetary Science Letters*, *311*(3–4), 242–252. https://doi.org/10.1016/j.epsl.2011.09.021

Baker, P. A., & Kastner, M. (1981). Constraints on the Formation of Sedimentary Dolomite. *Science*, *213*(4504), 214 LP – 216. https://doi.org/10.1126/science.213.4504.214

Barnes, I., & O'Neil, J. R. (1969). The relationship between fluids in some fresh alpine-type ultramafics and possible modern serpentinization, western United States. *Bulletin of the Geological Society of America*, *80*(10), 1947–1960. https://doi.org/10.1130/0016-7606(1969)80[1947:TRBFIS]2.0.CO;2

Barnes, I., LaMarche, V. C., & Himmelberg, G. (1967). Geochemical Evidence of Present-Day Serpentinization. *Science*, *156*(3776), 830–832. https://doi.org/10.1126/science.156.3776.830

Barnes, I., O'Neil, J. R., Rapp, J. B., & White, D. E. (1973). Silica-carbonate alteration of serpentine: Wall rock alteration in mercury deposits of the California Coast Ranges. *Economic Geology*, *68*(3), 388–398. https://doi.org/10.2113/gsecongeo.68.3.388

Barnes, I., O'Neil, J. R., & Trescases, J. J. (1978). Present day serpentinization in New Caledonia, Oman and Yugoslavia. *Geochimica et Cosmochimica Acta*, *42*(1), 144–145. https://doi.org/10.1016/0016-7037(78)90225-9

Barry, P. H., de Moor, J. M., Giovannelli, D., Schrenk, M. O., Hummer, D. R., Lopez, T., et al. (2019). Forearc carbon sink reduces long-term volatile recycling into the mantle. *Nature*, *568*(7753), 487–492. https://doi.org/10.1038/s41586-019-1131-5

Beinlich, A., Plümper, O., Hövelmann, J., Austrheim, H., & Jamtveit, B. (2012). Massive serpentinite carbonation at Linnajavri, N-Norway. *Terra Nova*, *24*(6), 446–455. https://doi.org/10.1111/j.1365-3121.2012.01083.x

Beinlich, A., John, T., Vrijmoed, J. C., Tominaga, M., Magna, T., & Podladchikov, Y. Y. (2020). Instantaneous rock transformations in the deep crust driven by reactive fluid flow. *Nature Geoscience*, *13*(4), 307–311. https://doi.org/10.1038/s41561-020-0554-9

Beinlich, A., Plümper, O., Boter, E., Müller, I. A., Kourim, F., Ziegler, M., et al. (2020). Ultramafic Rock Carbonation: Constraints From Listvenite Core BT1B, Oman Drilling Project. *Journal of Geophysical Research: Solid Earth*, *125*(6). https://doi.org/10.1029/2019JB019060

Bernasconi, S. M., Müller, I. A., Bergmann, K. D., Breitenbach, S. F. M., Fernández, Á., Hodell, D. A., et al. (2018). Reducing Uncertainties in Carbonate Clumped Isotope Analysis Through Consistent Carbonate-Based Standardization. *Geochemistry, Geophysics, Geosystems*, *19*(9), 2895–2914. https://doi.org/10.1029/2017GC007385

Bjerga, A., Konopásek, J., & Pedersen, R. B. (2015). Talc-carbonate alteration of ultramafic rocks within the Leka Ophiolite Complex, Central Norway. *Lithos*, *227*, 21–36. https://doi.org/10.1016/j.lithos.2015.03.016

Bosak, T., & Newman, D. K. (2003). Microbial nucleation of calcium carbonate in the Precambrian. *Geology*, *31*(7), 577–580. https://doi.org/10.1130/0091-7613(2003)031<0577:MNOCCI>2.0.CO;2

Boskabadi, A., Pitcairn, I. K., Leybourne, M. I., Teagle, D. A. H., Cooper, M. J., Hadizadeh, H., et al. (2020). Carbonation of ophiolitic ultramafic rocks: Listvenite formation in the Late Cretaceous ophiolites of eastern Iran. *Lithos*, *352–353*, 105307. https://doi.org/10.1016/j.lithos.2019.105307

Boudier, F., & Coleman, R. G. (1981). Cross Section Through the Peridotite in the Samail Ophiolite, Southeastern Oman Mountains, *86*(80), 2573–2592.

Bradley, A. S., Hayes, J. M., & Summons, R. E. (2009). Extraordinary 13C enrichment of diether lipids at the Lost City Hydrothermal Field indicates a carbon-limited ecosystem. *Geochimica et Cosmochimica Acta*, *73*(1), 102–118. https://doi.org/10.1016/j.gca.2008.10.005

Brady, P. V., Krumhansl, J. L., & Papenguth, H. W. (1996). Surface complexation clues to dolomite growth. *Geochimica et Cosmochimica Acta*, *60*(4), 727–731. https://doi.org/10.1016/0016-7037(95)00436-X

Braun, M. G. (2004). *Petrologic and Microstructural Constraints on Focused Melt Transport in Dunites and the Rheology of the Shallow Mantle*. *Supportive Care in Cancer*. MIT and Woods Hole Oceanographic Institute. https://doi.org/10.1007/s00520-004-0648-8

Braun, M. G., & Kelemen, P. B. (2002). Dunite distribution in the Oman Ophiolite: Implications for melt flux through porous dunite conduits. *Geochemistry, Geophysics, Geosystems*, *3*(11), 1–21. https://doi.org/10.1029/2001gc000289

Brazelton, W. J., Nelson, B., & Schrenk, M. O. (2012). Metagenomic evidence for H2 oxidation and H2 production by serpentinite-hosted subsurface microbial communities. *Frontiers in Microbiology*, *2*(JAN), 1–16. https://doi.org/10.3389/fmicb.2011.00268

Breitenbach, S. F. M., & Bernasconi, S. M. (2011). Carbon and oxygen isotope analysis of small carbonate samples (20 to 100 μg) with a GasBench II preparation device. *Rapid*

Communications in Mass Spectrometry, *25*(13), 1910–1914. https://doi.org/10.1002/rcm.5052

Bruni, J., Canepa, M., Chiodini, G., Cioni, R., Cipolli, F., Longinelli, A., et al. (2002). Irreversible water-rock mass transfer accompanying the generation of the neutral, Mg–HCO3 and high-pH, Ca–OH spring waters of the Genova province, Italy. *Applied Geochemistry*, *17*(4), 455–474. https://doi.org/10.1016/S0883-2927(01)00113-5

Cannat, M., Fontaine, F., & Escartín, J. (2010). Serpentinization and associated hydrogen and methane fluxes at slow-spreading ridges. In *Diversity of Hydrothermal Systems on Slow Spreading Ocean Ridges* (pp. 241–264). https://doi.org/10.1029/2008GM000760

Charlou, J. L., Donval, J. P., Fouquet, Y., Jean-Baptiste, P., & Holm, N. G. (2002). Geochemistry of high H2 and CH4 vent fluids issuing from ultramafic rocks at the Rainbow hydrothermal field (36°14′N, MAR). *Chemical Geology*, *191*(4), 345–359. https://doi.org/10.1016/S0009-2541(02)00134-1

Chavagnac, V., Monnin, C., Ceuleneer, G., Boulart, C., & Hoareau, G. (2013). Characterization of hyperalkaline fluids produced by low-temperature serpentinization of mantle peridotites in the Oman and Ligurian ophiolites. *Geochemistry, Geophysics, Geosystems*, *14*(7), 2496–2522. https://doi.org/10.1002/ggge.20147

Cipolli, F., Gambardella, B., Marini, L., Ottonello, G., & Zuccolini, M. V. (2004). Geochemistry of high-pH waters from serpentinites of the Gruppo di Voltri (Genova, Italy) and reaction path modeling of CO2 sequestration in serpentinite aquifers. *Applied Geochemistry*, *19*(5), 787–802. https://doi.org/10.1016/j.apgeochem.2003.10.007

Clark, I. D., & Fontes, J. C. (1990). Paleoclimatic reconstruction in northern Oman based on carbonates from hyperalkaline groundwaters. *Quaternary Research*, *33*(3), 320–336. https://doi.org/10.1016/0033-5894(90)90059-T

Clark, I. D., Fontes, J. C., & Fritz, P. (1992). Stable isotope disequilibria in travertine from high pH waters: Laboratory investigations and field observations from Oman. *Geochimica et Cosmochimica Acta*, *56*(5), 2041–2050. https://doi.org/10.1016/0016-7037(92)90328-G

Coleman, R. G. (1981). Tectonic setting for ophiolite obduction in Oman. *Journal of Geophysical Research: Solid Earth*, *86*(B4), 2497–2508. https://doi.org/10.1029/JB086iB04p02497

Colman, D. R., Poudel, S., Stamps, B. W., Boyd, E. S., & Spear, J. R. (2017). The deep, hot biosphere: Twenty-five years of retrospection. *Proceedings of the National Academy of Sciences of the United States of America*, *114*(27), 6895–6903. https://doi.org/10.1073/pnas.1701266114

Cowan, R. J., Searle, M. P., & Waters, D. J. (2014). Structure of the metamorphic sole to the Oman Ophiolite, Sumeini Window and Wadi Tayyin: Implications for ophiolite obduction processes. *Geological Society Special Publication*, *392*(1), 155–175. https://doi.org/10.1144/SP392.8

Curtis, A. C., Wheat, C. G., Fryer, P., & Moyer, C. L. (2013). Mariana Forearc Serpentinite Mud Volcanoes Harbor Novel Communities of Extremophilic Archaea. *Geomicrobiology Journal*, *30*(5), 430–441. https://doi.org/10.1080/01490451.2012.705226

Daae, F. L., Økland, I., Dahle, H., Jørgensen, S. L., Thorseth, I. H., & Pedersen, R. B. (2013). Microbial life associated with low-temperature alteration of ultramafic rocks in the Leka ophiolite complex. *Geobiology*, *11*(4), 318–339. https://doi.org/10.1111/gbi.12035

Delacour, A., Früh-Green, G. L., Bernasconi, S. M., Schaeffer, P., & Kelley, D. S. (2008). Carbon geochemistry of serpentinites in the Lost City Hydrothermal System (30°N, MAR). *Geochimica et Cosmochimica Acta*, *72*(15), 3681–3702. https://doi.org/10.1016/j.gca.2008.04.039

Delacour, A., Früh-Green, G. L., Bernasconi, S. M., & Kelley, D. S. (2008). Sulfur in peridotites and gabbros at Lost City (30°N, MAR): Implications for hydrothermal alteration and microbial activity during serpentinization. *Geochimica et Cosmochimica Acta*, *72*(20), 5090–5110. https://doi.org/10.1016/j.gca.2008.07.017

Deppenmeier, U., Müller, V., & Gottschalk, G. (1996). Pathways of energy conservation in methanogenic archaea. *Archives of Microbiology*, *165*(3), 149–163. https://doi.org/10.1007/s002030050310

Dewandel, B., Lachassagne, P., Boudier, F., Al-Hattali, S., Ladouche, B., Pinault, J. L., & Al-Suleimani, Z. (2005). A conceptual hydrogeological model of ophiolite hard-rock aquifers in Oman based on a multiscale and a multidisciplinary approach. *Hydrogeology Journal*, *13*(5–6), 708–726. https://doi.org/10.1007/s10040-005-0449-2

Dick, H. J. B., & Bullen, T. (1984). Chromian spinel as a petrogenetic indicator in abyssal and alpine-type peridotites and spatially associated lavas. *Contributions to Mineralogy and Petrology*, *86*(1), 54–76. https://doi.org/10.1007/BF00373711

Drake, H., Åström, M. E., Heim, C., Broman, C., Åström, J., Whitehouse, M., et al. (2015). Extreme 13C depletion of carbonates formed during oxidation of biogenic methane in fractured granite. *Nature Communications*, *6*(1), 7020. https://doi.org/10.1038/ncomms8020

Etiope, G., & Sherwood Lollar, B. (2013). Abiotic methane on earth. *Reviews of Geophysics*, *51*(2), 276–299. https://doi.org/10.1002/rog.20011

Falk, E. S., & Kelemen, P. B. (2015). Geochemistry and petrology of listvenite in the Samail ophiolite, Sultanate of Oman: Complete carbonation of peridotite during ophiolite emplacement. *Geochimica et Cosmochimica Acta*, *160*, 70–90. https://doi.org/10.1016/j.gca.2015.03.014

Falk, E. S., Guo, W., Paukert, A. N., Matter, J. M., Mervine, E. M., & Kelemen, P. B. (2016). Controls on the stable isotope compositions of travertine from hyperalkaline springs in Oman: Insights from clumped isotope measurements. *Geochimica et Cosmochimica Acta*, *192*, 1–28. https://doi.org/10.1016/j.gca.2016.06.026

Fernández, Á., Müller, I. A., Rodríguez-Sanz, L., van Dijk, J., Looser, N., & Bernasconi, S. M. (2017). A Reassessment of the Precision of Carbonate Clumped Isotope Measurements: Implications for Calibrations and Paleoclimate Reconstructions. *Geochemistry, Geophysics, Geosystems*, *18*(12), 4375–4386. https://doi.org/10.1002/2017GC007106

Fleitmann, D., Burns, S. J., Pekala, M., Mangini, A., Al-Subbary, A., Al-Aowah, M., et al. (2011). Holocene and Pleistocene pluvial periods in Yemen, southern Arabia. *Quaternary Science Reviews*, *30*(7–8), 783–787. https://doi.org/10.1016/j.quascirev.2011.01.004

Friedman, I., & O'Neil, J. R. (1977). Compilation of stable isotope fractionation factors of geochemical interest. In: Fleisher, M. (Ed.), Data of Geochemistry, 6th ed. *Geological Survey Professional Paper*, *440*, 1–12. https://doi.org/10.1016/S0016-0032(20)90415-5

Frost, R. B., & Beard, J. S. (2007). On silica activity and serpentinization. *Journal of Petrology*, *48*(7), 1351–1368. https://doi.org/10.1093/petrology/egm021

Fullerton, K., Schrenk, M. O., Yucel, M., Manini, E., Marco, B., Rogers, T., et al. (2019). Plate tectonics drive deep biosphere microbial community structure. *EarthArXiv*. https://doi.org/10.31223/osf.io/gyr7n

Gartzos, E. (2004). Compararative Stable Isotopes Study of the Magnesite Deposits of Greece. *Bulletin of the Geological Society of Greece*, *36*(1), 196. https://doi.org/10.12681/bgsg.16619

Gnos, E. (1998). Peak metamorphic conditions of garnet amphibolites beneath the semail ophiolite: Implications for an inverted pressure gradient. *International Geology Review*, *40*(4), 281–304. https://doi.org/10.1080/00206819809465210

Godard, M., Jousselin, D., & Bodinier, J. L. (2000). Relationships between geochemistry and structure beneath a palaeo-spreading centre: A study of the mantle section in the Oman ophiolite. *Earth and Planetary Science Letters*, *180*(1–2), 133–148. https://doi.org/10.1016/S0012-821X(00)00149-7

Godard, M., Dautria, J.-M., & Perrin, M. (2003). Geochemical variability of the Oman ophiolite lavas: Relationship with spatial distribution and paleomagnetic directions. *Geochemistry, Geophysics, Geosystems*, *4*(6), n/a-n/a. https://doi.org/10.1029/2002GC000452

Grossman, E. L., & Ku, T. L. (1986). Carbon and oxygen isotopic fractionation in biogenic aragonite-temp effects. *Chemical Geology*, *59*(April), 59–74. Retrieved from https://www.researchgate.net/publication/291049277

Hacker, B. R. (1994). Rapid emplacement of young oceanic lithosphere: Argon geochronology of the oman ophiolite. *Science*, *265*(5178), 1563–1565. https://doi.org/10.1126/science.265.5178.1563

Hacker, B. R., & Gnos, E. (1997). The corundum of semail: explaining the metamorphic history. *Tectonophysics*, *279*, 215–226.

Hacker, B. R., & Mosenfelder, J. L. (1996). Metamorphism and deformation along the emplacement thrust of the Samail ophiolite, Oman. *Earth and Planetary Science Letters*, *144*(3–4), 435–451. https://doi.org/10.1016/s0012-821x(96)00186-0

Hacker, B. R., Mosenfelder, J. L., & Gnos, E. (1996). Rapid emplacement of the Oman ophiolite: Thermal and geochronologic constraints. *Tectonics*, *15*(6), 1230–1247.

Halls, C., & Zhao, R. (1995). Listvenite and related rocks: perspectives on terminology and mineralogy with reference to an occurrence at Cregganbaun, Co. Mayo, Republic of Ireland. *Mineral Deposita*, *30*, 303–313.

Hanghoj, K., Kelemen, P. B., Hassler, D., & Godard, M. (2010). Composition and Genesis of Depleted Mantle Peridotites from the Wadi Tayin Massif, Oman Ophiolite; Major and Trace Element Geochemistry, and Os Isotope and PGE Systematics. *Journal of Petrology*, *51*(1–2), 201–227. https://doi.org/10.1093/petrology/egp077

Hu, B., Radke, J., Schlüter, H.-J., Heine, F. T., Zhou, L., & Bernasconi, S. M. (2014). A modified procedure for gas-source isotope ratio mass spectrometry: the long-integration dual-inlet (LIDI) methodology and implications for clumped isotope measurements. *Rapid Communications in Mass Spectrometry*, *28*(13), 1413–1425. https://doi.org/10.1002/rcm.6909

Jedrysek, M. O., & Sachanbinski, M. (1994). Stable isotope and trace element studies of vein ophicarbonates at Gogolow-Jordanow serpentinite massif (Poland): A contribution to the origin of ophiaragonite and ophimagnesite. *GEOCHEMICAL JOURNAL*, *28*(4), 341–350. https://doi.org/10.2343/geochemj.28.341

Katayama, I., Abe, N., Hatakeyama, K., Akamatsu, Y., Okazaki, K., Ulven, O. I., et al. (2020). Permeability Profiles Across the Crust-Mantle Sections in the Oman Drilling Project Inferred From Dry and Wet Resistivity Data. *Journal of Geophysical Research: Solid Earth*, *125*(8), 1–9. https://doi.org/10.1029/2019JB018698

Kelemen, P. B., & Matter, J. M. (2008). In situ carbonation of peridotite for CO2 storage. *Proceedings of the National Academy of Sciences of the United States of America*, *105*(45), 17295–17300. https://doi.org/10.1073/pnas.0805794105

Kelemen, P. B., Shimizu, N., & Salters, V. J. M. (1995). Extraction of mid-ocean-ridge basalt from the upwelling mantle by focused flow of melt in dunite channels. *Nature*, *375*(6534), 747–753. https://doi.org/10.1038/375747a0

Kelemen, P. B., Matter, J. M., Streit, E. E., Rudge, J. F., Curry, W. B., & Blusztajn, J. S. (2011). Rates and Mechanisms of Mineral Carbonation in Peridotite: Natural Processes and Recipes for Enhanced, in situ CO 2 Capture and Storage. *Annual Review of Earth and Planetary Sciences*, *39*(1), 545–576. https://doi.org/10.1146/annurev-earth-092010-152509

Kelemen, P. B., Matter, J. M., Teagle., D. A. H., Coggon., J. A., & Science Team., the O. D. P. (2020). Methods and explanatory notes. *Proceedings of the Oman Drilling Project: College Station, TX (International Ocean Discovery Program)*, (May), 1–173. Retrieved from http://publications.iodp.org/other/Oman/OmanDP.html

Kelemen, P. B., Matter, J. M., Teagle, D. A. H., Coggan, J. A., & the Oman Drilling Project Science Team. (2020). *Proceedings of the Oman Drilling Project*. College Station, TX: International Ocean Discovery Program. https://doi.org/10.14379/OmanDP.proc.2020

Kelley, D. S., & Früh-Green, G. L. (2001). Volatile lines of descent in submarine plutonic environments: Insights from stable isotope and fluid inclusion analyses. *Geochimica et Cosmochimica Acta*, *65*(19), 3325–3346. https://doi.org/10.1016/S0016-7037(01)00667-6

Kelley, D. S., Karson, J. A., Früh-Green, G. L., Yoerger, D. R., Shank, T. M., Butterfield, D. A., et al. (2005). A Serpentinite-Hosted Ecosystem: The Lost City Hydrothermal Field. *Science*, *307*(5714), 1428–1434. https://doi.org/10.1126/science.1102556

Kenward, P. A., Goldstein, R. H., GonzÁlez, L. A., & Roberts, J. A. (2009). Precipitation of low-temperature dolomite from an anaerobic microbial consortium: The role of methanogenic Archaea. *Geobiology*, *7*(5), 556–565. https://doi.org/10.1111/j.1472-4669.2009.00210.x

Konn, C., Charlou, J. L., Holm, N. G., & Mousis, O. (2015). The production of methane, hydrogen, and organic compounds in ultramafic-hosted hydrothermal vents of the mid-atlantic ridge. *Astrobiology*, *15*(5), 381–399. https://doi.org/10.1089/ast.2014.1198

Kourkoumelis, N. (2013). PowDLL, a reusable .NET component for interconverting powder diffraction data: Recent developments. In L. O'Neill (Ed.), *ICDD Annual Spring Meetings* (Vol. 28, pp. 137–48).

Labidi, J., Young, E. D., Giunta, T., Kohl, I. E., Seewald, J. S., Tang, H., et al. (2020). Methane thermometry in deep-sea hydrothermal systems: evidence for re-ordering of doubly-substituted isotopologues during fluid cooling. https://doi.org/10.1017/CBO9781107415324.004

Lafuente, B., Downs, R. T., Yang, H., & Stone, N. (2015). 1. The power of databases: The RRUFF project. In T. Armbruster & R. M. Danisi (Eds.), *Highlights in Mineralogical Crystallography* (pp. 1–30). Berlin, München, Boston: De Gruyter (O). https://doi.org/10.1515/9783110417104-003

Lang, S. Q., Früh-Green, G. L., Bernasconi, S. M., Brazelton, W. J., Schrenk, M. O., & McGonigle, J. M. (2018). Deeply-sourced formate fuels sulfate reducers but not methanogens at Lost City hydrothermal field. *Scientific Reports*, *8*(1), 1–10. https://doi.org/10.1038/s41598-017-19002-5

Lanphere, M. A. (1981). K-Ar ages of metamorphic rocks at the base of the Samail ophiolite, Oman. *Journal of Geophysical Research*, *86*(B4), 2777–2782. https://doi.org/10.1029/JB086iB04p02777

Lincoln, S. A., Bradley, A. S., Newman, S. A., & Summons, R. E. (2013). Archaeal and bacterial glycerol dialkyl glycerol tetraether lipids in chimneys of the Lost City Hydrothermal Field. *Organic Geochemistry*, *60*, 45–53. https://doi.org/10.1016/j.orggeochem.2013.04.010

Lister, C. R. B. (1972). On the thermal balance of a mid-ocean ridge. *Geophys. J. R. Astron. Soc.*, *26*, 515–535.

McCollom, T. M., & Bach, W. (2009). Thermodynamic constraints on hydrogen generation during serpentinization of ultramafic rocks. *Geochimica et Cosmochimica Acta*, *73*(3), 856–875. https://doi.org/10.1016/j.gca.2008.10.032

McCollom, T. M., & Seewald, J. S. (2006). Carbon isotope composition of organic compounds produced by abiotic synthesis under hydrothermal conditions. *Earth and Planetary Science Letters*, *243*(1–2), 74–84. https://doi.org/10.1016/j.epsl.2006.01.027

Meckler, A. N., Ziegler, M., Millán, M. I., Breitenbach, S. F. M., & Bernasconi, S. M. (2014). Long-term performance of the Kiel carbonate device with a new correction scheme for clumped isotope measurements. *Rapid Communications in Mass Spectrometry*, *28*(15), 1705–1715. https://doi.org/10.1002/rcm.6949

Le Mée, L., Girardeau, J., & Monnier, C. (2004). Mantle segmentation along the Oman ophiolite fossil mid-ocean ridge. *Nature*, *432*(7014), 167–172. https://doi.org/10.1038/nature03075

Méhay, S., Früh-Green, G. L., Lang, S. Q., Bernasconi, S. M., Brazelton, W. J., Schrenk, M. O., et al. (2013). Record of archaeal activity at the serpentinite-hosted Lost City Hydrothermal Field. *Geobiology*, *11*(6), 570–592. https://doi.org/10.1111/gbi.12062

Menzel, M. D., Garrido, C. J., López Sánchez-Vizcaíno, V., Marchesi, C., Hidas, K., Escayola, M. P., & Delgado Huertas, A. (2018). Carbonation of mantle peridotite by CO2-rich fluids: the formation of listvenites in the Advocate ophiolite complex (Newfoundland, Canada). *Lithos*, *323*, 238–261. https://doi.org/10.1016/j.lithos.2018.06.001

Mervine, E. M., Humphris, S. E., Sims, K. W. W., Kelemen, P. B., & Jenkins, W. J. (2014). Carbonation rates of peridotite in the Samail Ophiolite, Sultanate of Oman, constrained through 14C dating and stable isotopes. *Geochimica et Cosmochimica Acta*, *126*, 371–397. https://doi.org/10.1016/j.gca.2013.11.007

Miller, H. M., Matter, J. M., Kelemen, P. B., Ellison, E. T., Conrad, M. E., Fierer, N., et al. (2016). Modern water/rock reactions in Oman hyperalkaline peridotite aquifers and implications for microbial habitability. *Geochimica et Cosmochimica Acta*, *179*, 217–241. https://doi.org/10.1016/j.gca.2016.01.033

Miura, M., Arai, S., & Mizukami, T. (2011). Raman spectroscopy of hydrous inclusions in olivine and orthopyroxene in ophiolitic harzburgite: Implications for elementary processes in serpentinization. *Journal of Mineralogical and Petrological Sciences*, *106*(2), 91–96. https://doi.org/10.2465/jmps.101021d

Monnier, C., Girardeau, J., Le Mée, L., & Polvé, M. (2006). Along-ridge petrological segmentation of the mantle in the Oman ophiolite. *Geochemistry, Geophysics, Geosystems*, *7*(11). https://doi.org/10.1029/2006GC001320

Moore, T. S., Murray, R. W., Kurtz, A. C., & Schrag, D. P. (2004). Anaerobic methane oxidation and the formation of dolomite. *Earth and Planetary Science Letters*, *229*(1–2), 141–154. https://doi.org/10.1016/j.epsl.2004.10.015

Moreira, N. F., Walter, L. M., Vasconcelos, C., McKenzie, J. A., & McCall, P. J. (2004). Role of sulfide oxidation in dolomitization: Sediment and pore-water geochemistry of a modern hypersaline lagoon system. *Geology*, *32*(8), 701. https://doi.org/10.1130/G20353.1

Mottl, M. J., Komor, S. C., Fryer, P., & Moyer, C. L. (2003). Deep-slab fluids fuel extremophilic Archaea on a Mariana forearc serpentinite mud volcano: Ocean drilling program leg 195. *Geochemistry, Geophysics, Geosystems*, *4*(11), 1–14. https://doi.org/10.1029/2003GC000588

Müller, I. A., Fernández, Á., Radke, J., van Dijk, J., Bowen, D., Schwieters, J., & Bernasconi, S. M. (2017). Carbonate clumped isotope analyses with the long-integration dual-inlet (LIDI) workflow: scratching at the lower sample weight boundaries. *Rapid Communications in Mass Spectrometry*, *31*(12), 1057–1066. https://doi.org/10.1002/rcm.7878

Müller, I. A., Rodriguez-Blanco, J. D., Storck, J.-C., do Nascimento, G. S., Bontognali, T. R. R., Vasconcelos, C., et al. (2019). Calibration of the oxygen and clumped isotope thermometers for (proto-)dolomite based on synthetic and natural carbonates. *Chemical Geology*, *525*(December 2018), 1–17. https://doi.org/10.1016/j.chemgeo.2019.07.014

Nasir, S., Al Sayigh, A. R., Al Harthy, A., Al-Khirbash, S., Al-Jaaidi, O., Musllam, A., et al. (2007). Mineralogical and geochemical characterization of listwaenite from the Semail Ophiolite, Oman. *Chemie Der Erde*, *67*(3), 213–228. https://doi.org/10.1016/j.chemer.2005.01.003

Neal, C., & Stanger, G. (1983). Hydrogen generation from mantle source rocks in Oman. *Earth and Planetary Science Letters*, *66*(C), 315–320. https://doi.org/10.1016/0012-821X(83)90144-9

Neal, C., & Stanger, G. (1985). Past And Present Serpentinisation of Ultramafic Rocks; An Example from the Semail Ophiolite Nappe of Northern Oman BT - The Chemistry of Weathering. In J. I. Drever (Ed.) (pp. 249–275). Dordrecht: Springer Netherlands. https://doi.org/10.1007/978-94-009-5333-8_15

Newman, S. A., Lincoln, S. A., O'Reilly, S., Liu, X., Shock, E. L., Kelemen, P. B., & Summons, R. E. (2020). Lipid Biomarker Record of the Serpentinite-Hosted Ecosystem of the Samail Ophiolite, Oman and Implications for the Search for Biosignatures on Mars. *Astrobiology*, *20*(7), 830–845. https://doi.org/10.1089/ast.2019.2066

Nicholson, S. L., Pike, A. W. G., Hosfield, R., Roberts, N., Sahy, D., Woodhead, J., et al. (2020). Pluvial periods in Southern Arabia over the last 1.1 million-years. *Quaternary Science Reviews*, *229*. https://doi.org/10.1016/j.quascirev.2019.106112

Nicolas, A. (1989). *Structures of Ophiolites and Dynamics of Oceanic Lithosphere* (Vol. 4). Dordrecht: Springer Netherlands. https://doi.org/10.1007/978-94-009-2374-4

Nicolas, A., Boudier, F., Ildefonse, B., & Ball, E. (2000). Accretion of Oman and United Arab Emirates ophiolite – Discussion of a new structural map. *Marine Geophysical Researches*, *21*(3/4), 147–180. https://doi.org/10.1023/A:1026769727917

Noël, J., Godard, M., Oliot, E., Martinez, I., Williams, M. J., Boudier, F., et al. (2018). Evidence of polygenetic carbon trapping in the Oman Ophiolite: Petro-structural, geochemical, and carbon and oxygen isotope study of the Wadi Dima harzburgite-hosted carbonates (Wadi Tayin massif, Sultanate of Oman). *Lithos*, *323*, 218–237. https://doi.org/10.1016/j.lithos.2018.08.020

Nothaft, D. B., Templeton, A. S., Rhim, J. H., Wang, D. T., Labidi, J., Miller, H. M., et al. (2020). Geochemical , biological and clumped isotopologue evidence for substantial microbial methane production under carbon limitation in serpentinites of the Samail Opiolite, Oman. *JGR: Biogeosciences*.

O'Neil, J. R., & Barnes, I. (1971). C13 and O18 compositions in some fresh-water carbonates associated with ultramafic rocks and serpentinites: western United States. *Geochimica et Cosmochimica Acta*, *35*(7), 687–697. https://doi.org/10.1016/0016-7037(71)90067-6

O'Neil, J. R., Clayton, R. N., & Mayeda, T. K. (1969). Oxygen isotope fractionation in divalent metal carbonates. *The Journal of Chemical Physics*, *51*(12), 5547–5558. https://doi.org/10.1063/1.1671982

Ohara, Y., Reagan, M. K., Fujikura, K., Watanabe, H., Michibayashi, K., Ishii, T., et al. (2012). A serpentinite-hosted ecosystem in the Southern Mariana Forearc. *Proceedings of the National Academy of Sciences of the United States of America*, *109*(8), 2831–5. https://doi.org/10.1073/pnas.1112005109

Palandri, J. L., & Reed, M. H. (2004). Geochemical models of metasomatism in ultramafic systems: Serpentinization, rodingitization, and sea floor carbonate chimney precipitation. *Geochimica et Cosmochimica Acta*, *68*(5), 1115–1133. https://doi.org/10.1016/j.gca.2003.08.006

Pallister, J. S., & Knight, R. J. (1981). Rare-Earth Geochemistry of the Samail Ophiolite near Ibra, Oman. *Journal of Geophysical Research*, *86*(80), 2673–2697.

Paukert, A. N., Matter, J. M., Kelemen, P. B., Shock, E. L., & Havig, J. R. (2012). Reaction path modeling of enhanced in situ CO 2 mineralization for carbon sequestration in the peridotite of the Samail Ophiolite, Sultanate of Oman. *Chemical Geology*, *330–331*, 86–100. https://doi.org/10.1016/j.chemgeo.2012.08.013

Paukert Vankeuren, A. N., Matter, J. M., Stute, M., & Kelemen, P. B. (2019). Multitracer determination of apparent groundwater ages in peridotite aquifers within the Samail ophiolite, Sultanate of Oman. *Earth and Planetary Science Letters*, *516*, 37–48. https://doi.org/10.1016/j.epsl.2019.03.007

Pedersen, K., Ekendahl, S., Tullborg, E.-L., Furnes, H., Thorseth, I., & Tumyr, O. (1997). Evidence of ancient life at 207 m depth in a granitic aquife. *Geology*, *25*(9), 827. https://doi.org/10.1130/0091-7613(1997)025<0827:EOALAM>2.3.CO;2

Quesnel, B., Gautier, P., Boulvais, P., Cathelineau, M., Maurizot, P., Cluzel, D., et al. (2013). Syn-tectonic, meteoric water-derived carbonation of the New Caledonia peridotite nappe. *Geology*, *41*(10), 1063–1066. https://doi.org/10.1130/G34531.1

Quesnel, B., Boulvais, P., Gautier, P., Cathelineau, M., John, C. M., Dierick, M., et al. (2016). Paired stable isotopes (O, C) and clumped isotope thermometry of magnesite and silica veins in the New Caledonia Peridotite Nappe. *Geochimica et Cosmochimica Acta*, *183*, 234–249. https://doi.org/10.1016/j.gca.2016.03.021

Rabu, D., Nehlig, P., Roger, J., Béchennec, F., Beurrier, M., Le Métour, J., et al. (1993). *Stratigraphy and structure of the Oman mountains*.

Ravaut, P., Bayer, R., Hassani, R., Rousset, D., & Al Yahya'Ey, A. (1997). Structure and evolution of the northern Oman margin: Gravity and seismic constraints over the Zagros-Makran-Oman collision zone. *Tectonophysics*, *279*(1–4), 253–262. https://doi.org/10.1016/S0040-1951(97)00125-X

Reimer, P. J., Brown, T. A., & Reimer, Ron, W. (2004). Discussion: Reporting and calibration of post-bomb 14C data. *Radiocarbon*, *46*(1), 1111–1150. Retrieved from http://scholar.google.com/scholar?hl=en&btnG=Search&q=intitle:Intcal09+and+Marine09+radiocarbon+age+calibration+curves,+0-50,000+years+cal+BP#0

Rioux, M., Bowring, S. A., Kelemen, P. B., Gordon, S., Dudás, F., & Miller, R. (2012). Rapid crustal accretion and magma assimilation in the Oman-U.A.E. ophiolite: High precision U-Pb zircon geochronology of the gabbroic crust. *Journal of Geophysical Research: Solid Earth*, *117*(B7), n/a-n/a. https://doi.org/10.1029/2012JB009273

Rioux, M., Bowring, S. A., Kelemen, P. B., Gordon, S., Miller, R., & Dudás, F. (2013). Tectonic development of the Samail ophiolite: High-precision U-Pb zircon geochronology and Sm-Nd isotopic constraints on crustal growth and emplacement. *Journal of Geophysical Research: Solid Earth*, *118*(5), 2085–2101. https://doi.org/10.1002/jgrb.50139

Rioux, M., Garber, J., Bauer, A., Bowring, S. A., Searle, M. P., Kelemen, P. B., & Hacker, B. R. (2016). Synchronous formation of the metamorphic sole and igneous crust of the Semail ophiolite: New constraints on the tectonic evolution during ophiolite formation from high-precision U–Pb zircon geochronology. *Earth and Planetary Science Letters*, *451*, 185–195. https://doi.org/10.1016/j.epsl.2016.06.051

Rozanski, K., Araguás-Araguás, L., & Gonfiantini, R. (1993). Isotopic Patterns in Modern Global Precipitation. In *Climate Change in Continental Isotopic Records. In: Americn Geophysical Union Geophysical Monograph 78*. https://doi.org/10.1029/GM078p0001

Ruff, M., Szidat, S., Gäggeler, H. W., Suter, M., Synal, H. A., & Wacker, L. (2010). Gaseous radiocarbon measurements of small samples. *Nuclear Instruments and Methods in Physics Research, Section B: Beam Interactions with Materials and Atoms*, *268*(7–8), 790–794. https://doi.org/10.1016/j.nimb.2009.10.032

Sánchez-Román, M., McKenzie, J. A., de Luca Rebello Wagener, A., Rivadeneyra, M. A., & Vasconcelos, C. (2009). Presence of sulfate does not inhibit low-temperature dolomite precipitation. *Earth and Planetary Science Letters*, *285*(1–2), 131–139. https://doi.org/10.1016/j.epsl.2009.06.003

Schrenk, M. O., Brazelton, W. J., & Lang, S. Q. (2013). Serpentinization, carbon, and deep life. *Reviews in Mineralogy and Geochemistry*, *75*, 575–606. https://doi.org/10.2138/rmg.2013.75.18

Schroeder, T. J., Bach, W., Jöns, N., Jöns, S., Monien, P., & Klügel, A. (2015). Fluid circulation and carbonate vein precipitation in the footwall of an oceanic core complex, Ocean Drilling Program Site 175, Mid-Atlantic Ridge. *Geochemistry, Geophysics, Geosystems*, *16*(10), 3716–3732. https://doi.org/10.1002/2015GC006041

Schwarzenbach, E. M., Früh-Green, G. L., Bernasconi, S. M., Alt, J. C., & Plas, A. (2013). Serpentinization and carbon sequestration: A study of two ancient peridotite-hosted hydrothermal systems. *Chemical Geology*, *351*, 115–133. https://doi.org/10.1016/j.chemgeo.2013.05.016

Schwarzenbach, E. M., Lang, S. Q., Früh-Green, G. L., Lilley, M. D., Bernasconi, S. M., & Méhay, S. (2013). Sources and cycling of carbon in continental, serpentinite-hosted alkaline springs in the Voltri Massif, Italy. *Lithos*, *177*, 226–244. https://doi.org/10.1016/j.lithos.2013.07.009

Scicchitano, M. R., Spicuzza, M. J., Ellison, E. T., Tuschel, D., Templeton, A. S., & Valley, J. W. (2020). In Situ Oxygen Isotope Determination in Serpentine Minerals by SIMS: Addressing Matrix Effects and Providing New Insights on Serpentinisation at Hole BA1B (Samail ophiolite, Oman). *Geostandards and Geoanalytical Research*, (2), ggr.12359. https://doi.org/10.1111/ggr.12359

Searle, M. P., & Malpas, J. (1980). Structure and metamorphism of rocks beneath the Semail ophiolite of Oman and their significance in ophiolite obduction. *Transactions of the Royal Society of Edinburgh: Earth Sciences*, *71*(4), 247–262. https://doi.org/10.1017/S0263593300013614

Searle, M. P., Waters, D. J., Garber, J., Rioux, M., Cherry, A. G., & Ambrose, T. K. (2015). Structure and metamorphism beneath the obducting Oman ophiolite: Evidence from the

Bani Hamid granulites, northern Oman mountains. *Geosphere*, *11*(6), 1812–1836. https://doi.org/10.1130/GES01199.1

Shanks, W. C., Böhlke, J. K., & Seal, R. R. (1995). Stable isotopes in mid-ocean ridge hydrothermal systems: interactions between fluids, minerals, and organisms. *SeaBoor Hydrothermal Systems: Physical, Chemical, Biological, and Geological Interactions*, *70*, 194–221.

Sibley, D. F., Dedoes, R. E., & Bartlett, T. R. (1987). Kinetics of dolomitization. *Geology*, *15*(12), 1112. https://doi.org/10.1130/0091-7613(1987)15<1112:KOD>2.0.CO;2

Stanger, G. (1985). Silicified serpentinite in the Semail nappe of Oman. *Lithos*, *18*(C), 13–22. https://doi.org/10.1016/0024-4937(85)90003-9

Streit, E. E., Kelemen, P. B., & Eiler, J. M. (2012). Coexisting serpentine and quartz from carbonate-bearing serpentinized peridotite in the Samail Ophiolite, Oman. *Contributions to Mineralogy and Petrology*, *164*(5), 821–837. https://doi.org/10.1007/s00410-012-0775-z

Synal, H. A., Stocker, M., & Suter, M. (2007). MICADAS: A new compact radiocarbon AMS system. *Nuclear Instruments and Methods in Physics Research, Section B: Beam Interactions with Materials and Atoms*, *259*(1), 7–13. https://doi.org/10.1016/j.nimb.2007.01.138

Ternieten, L., Früh-Green, G. L., & Bernasconi, S. M. (2021). Distribution and Sources of Carbon in Serpentinized Mantle Peridotites at the Atlantis Massif (IODP Expedition 357). https://doi.org/10.1002/essoar.10506361.1

Tilton, G. R., Hopson, C. A., & Wright, J. E. (1981). Uranium-lead isotopic ages of the Samail ophiolite, Oman, with applications to Tethyan ocean ridge tectonics. *Journal of Geophysical Research*, *86*(B4), 2763–2775. https://doi.org/10.1029/JB086iB04p02763

Vasconcelos, C., Mckenzie, J. A., Bernasconi, S., Grujic, D., & Tien, A. J. (1995). Microbial mediation as a possible mechanism for natural dolomite formation at low temperatures. *Nature*, *377*(September), 220–222.

Wacker, L., Bonani, G., Friedrich, M., Hajdas, I., Kromer, B., Němec, M., et al. (2010). Micadas: Routine and high-precision radiocarbon dating. *Radiocarbon*, *52*(2), 252–262. https://doi.org/10.1017/S0033822200045288

Wang, D. T., Reeves, E. P., McDermott, J. M., Seewald, J. S., & Ono, S. (2018). Clumped isotopologue constraints on the origin of methane at seafloor hot springs. *Geochimica et Cosmochimica Acta*, *223*, 141–158. https://doi.org/10.1016/j.gca.2017.11.030

Warren, C. J., Parrish, R. R., Waters, D. J., & Searle, M. P. (2005). Dating the geologic history of Oman's Semail ophiolite: Insights from U-Pb geochronology. *Contributions to Mineralogy and Petrology*, *150*(4), 403–422. https://doi.org/10.1007/s00410-005-0028-5

Weyhenmeyer, C. E., Burns, S. J., Waber, H. N., Aeschbach-Hertig, W., Kipfer, R., Loosli, H. H., & Matter, A. (2000). Cool glacial temperatures and changes in moisture source recorded in Oman groundwaters. *Science*, *287*(5454), 842–845. https://doi.org/10.1126/science.287.5454.842

Weyhenmeyer, C. E., Burns, S. J., Waber, H. N., Macumber, P. G., & Matter, A. (2002). Isotope study of moisture sources, recharge areas, and groundwater flow paths within the eastern Batinah coastal plain, sultanate of Oman. *Water Resources Research*, *38*(10), 2-1-2–22. https://doi.org/10.1029/2000wr000149

Wheat, C. G., & Mottl, M. J. (2004). Geochemical fluxes through mid-ocean ridge flanks. *In Hydrogeology of the Oceanic Lithosphere*, 627–658.

Zeebe, R. E. (2020). Oxygen isotope fractionation between water and the aqueous hydroxide ion. *Geochimica et Cosmochimica Acta*, *289*, 182–195. https://doi.org/10.1016/j.gca.2020.08.025